JCB Journal of Cell Biology

ARTICLE

An intrinsic compartmentalization code for peripheral membrane proteins in photoreceptor neurons

Nycole A. Maza[1,2], William E. Schiesser[3], and Peter D. Calvert[1,2]

In neurons, peripheral membrane proteins are enriched in subcellular compartments, where they play key roles, including transducing and transmitting information. However, little is known about the mechanisms underlying their compartmentalization. To explore the roles of hydrophobic and electrostatic interactions, we engineered probes consisting of lipidation motifs attached to fluorescent proteins by variously charged linkers and expressed them in *Xenopus* rod photoreceptors. Quantitative live cell imaging showed dramatic differences in distributions and dynamics of the probes, including presynapse and ciliary OS enrichment, depending on lipid moiety and protein surface charge. Opposing extant models of ciliary enrichment, most probes were weakly membrane bound and diffused through the connecting cilium without lipid binding chaperone protein interactions. A diffusion-binding-transport model showed that ciliary enrichment of a rhodopsin kinase probe occurs via recycling as it perpetually leaks out of the ciliary OS. The model accounts for weak membrane binding of peripheral membrane proteins and a leaky connecting cilium diffusion barrier.

Introduction

Neurons are highly polarized cells with distinct domains that receive and transmit signals. Proper function of neurons thus relies on correct distribution of proteins into functional compartments. Defects in protein trafficking are associated with devastating neurodegeneration or dysfunction. The mechanisms underlying the differential distribution of proteins in neurons are, thus, of fundamental importance. Trafficking of intrinsic membrane proteins has been well studied (reviewed in Bentley and Banker, 2016). How compartmentalization of peripheral membrane proteins (PMPs) is achieved, however, is poorly understood.

Posttranslational lipid modifications have emerged as an important mechanism for PMP localization to specific compartments (El-Husseini et al., 2000; Kerov et al., 2007). Three main types of protein lipidation are myristoylation, prenylation, and palmitoylation. In neuronal protein trafficking, the role of reversible protein palmitoylation is the most well characterized (reviewed in Fukata and Fukata, 2010). Less is known about the roles of N-terminal acylation and prenylation, irreversible forms of lipidation, in targeting PMPs to their functional compartments. In vitro, prenyl and acyl lipid modifications impart relatively weak membrane association on their own (Peitzsch and McLaughlin, 1993). Other properties of PMPs, including surface charge and/or association with other intrinsic cell structures, are needed to provide significant membrane association (Hancock et al., 1990; Murray et al., 1997; Resh, 2016). However, it is not known if acyl or prenyl moieties and surface charge are sufficient, on their own, to produce differential compartmentalization of PMPs in living neurons, or how this localization occurs.

In this study we addressed the roles of prenylation, acylation, and electrostatic charge on the subcellular enrichment and dynamics of PMPs in a sensory neuron, the retinal rod photoreceptor. Rods have three main compartments—the ciliary outer segment (OS), which is packed with membranous discs and phototransduction proteins, the presynaptic spherule, and the cell body. Targeting of some intrinsic membrane proteins to the OS and cell body has been addressed (Baker et al., 2008; Deretic and Wang, 2012; Lodowski et al., 2013; Wang and Deretic, 2014). However, aside from several studies examining the roles of lipid binding chaperone (LBC) proteins (Zhang et al., 2011, 2012; Thomas et al., 2014; Hanke-Gogokhia et al., 2016; Rainy et al.,

[1]Center for Vision Research, Department of Ophthalmology and Visual Sciences, State University of New York Upstate Medical University, Syracuse, NY; [2]Department of Neuroscience and Physiology, State University of New York Upstate Medical University, Syracuse, NY; [3]Department of Chemical and Biomolecular Engineering, Lehigh University, Bethlehem, PA.

Correspondence to Peter D. Calvert: calvertp@upstate.edu; N.A. Maza's present address is Department of Neuroscience, Scripps Research Institute, Jupiter, FL.

2016), the mechanisms underlying the subcellular localization of PMPs to specific rod compartments are not known. Here we show that lipid modification and nearby electrostatic charge alone result in dramatic differential distribution of PMPs, and we propose a mechanism for regulating their enrichment within, or depletion from, photoreceptor cilia. Lipid moiety and surface charge thus constitute an intrinsic compartmentalization code for PMPs in photoreceptors.

Results

Lipid modification and surface charge alone lead to compartment enrichment of PMPs in rods

To evaluate the roles of lipid modification and protein surface charge on PMP distribution in rods, we engineered fluorescent protein probes consisting of short peptides containing different lipidation motifs and charged or neutral amino acids, fused to EGFP or its photoactivatable variant, PAGFP (Fig. 1 A). The probes did not contain known binding motifs for phototransduction or LBC proteins so that the distribution patterns observed upon expression in *Xenopus laevis* rods would be the result of probe electrostatic and hydrophobic interactions with cell structures. Three probes derived from endogenous lipidated proteins, the α and γ subunits of the G protein supporting phototransduction, transducin (Tα and Tγ), and rhodopsin kinase (GRK1), the G protein receptor kinase involved in halting phototransduction, were generated as well. Distributions of the probes were evaluated by confocal imaging of live retinal explant slices (Fig. 1, B and C). Fig. 1 D shows the structures of the lipid moieties appended to the probes and estimates of their membrane binding energies and dissociation constants.

Remarkably, the probes displayed highly divergent distribution patterns among the rod compartments (Fig. 2, A and B). Relative enrichment of the probes within the two major functional compartments, the ciliary OS and the synapse, were quantified next (Fig. 2 C). Non-lipidated, neutrally charged probe (NL0) served as a benchmark, accounting for effects of protein size and steric interactions (Najafi et al., 2012). Positive charge–bearing prenylated probes were enriched within the synapse to a degree that depended on charge magnitude, with enrichment of +8 probes reaching >10-fold. Acylated probes, on the other hand, showed no significant difference in the synapse/OS ratio, regardless of linker charge (Fig. 2 C). Controls showed that probes with charged linkers and no lipid did not result in synaptic or OS enrichment (Figs. 2 B and 3 A) and that the addition of 21 amino acid linkers to C or N termini of EGFP did not impact the distribution (Fig. S1). Dramatic differences in the enrichment of PMPs between the two major functional rod compartments thus appeared to be encoded by lipid modification and protein surface charge alone.

Synaptic enrichment of positively charged prenylated probes is the result of OS depletion

To obtain a finer grain view of the differences in compartment enrichment, we evaluated probe distribution profiles within five subcellular domains: the synapse, nucleus, myoid, ellipsoid, and OS (Fig. 3). NL0 was broadly distributed throughout the cell, with the synaptic, nucleus, and myoid regions approximately uniformly filled and the ellipsoid and OSs containing twofold or lower fluorescence (Fig. 3 A), in agreement with our previous results (Peet et al., 2004; Calvert et al., 2010; Najafi et al., 2012). The distributions of the prenylated probes, on the other hand, were not uniform (Fig. 3, B and C). The concentration of prenyl probes was significantly lower in the nucleus than in any of the other cell body/inner segment (IS) compartments, a result that holds for all the lipidated probes in this study. Importantly, the distribution patterns did not change over at least a decade of expression (Fig. S2), indicating that differences were not due to saturation of binding or other nonspecific interactions.

The OS concentrations of prenylated probes with positively charged linkers were more than fivefold lower than the IS concentrations (Fig. 3 B). The concentration in the synapse was slightly higher on average than the myoid or ellipsoid. The neutral or negatively charged prenylated probes were present in the OS at higher concentrations (Fig. 3 C). Neutral probes often appeared in a concentration gradient from OS base to tip, and synaptic enrichment was less prominent.

To quantify the differences in distribution among the major rod compartments, we chose to compare the concentrations of the probes relative to the myoid, which serves as the protein synthesis and processing center of rods (Fig. 3, D and E). We refer to the concentration ratios as the OS (OSEI) or synapse enrichment indices (SynEI). Remarkably, positive prenyl probe OSEIs were seven-, five-, and threefold below that of NL0 (Fig. 3 D) and thus were depleted from the OS.

Nearly the opposite pattern was found for synaptic enrichment. SynEIs for positively charged prenyl probes were ∼1.6-fold greater for the +8 probes and 1.2-fold for the Far+4 probe, values that were significantly different from NL0. SynEIs for negatively charged probes were not significantly different from NL0 (Fig. 3 E). Of note, the magnitude of the SynEIs, maximally 1.6, was significantly below the up to sevenfold OS depletion. These results show that the >10-fold enrichment of positively charged prenylated probes in the presynapse relative to the OS was mostly due to depletion of the probes from the OS.

Positively charged prenyl probes are enriched in the IS plasma membrane, apical membrane region, and perinuclear membrane

In addition to enrichment in the synaptic spherule, prenyl +8 probes appeared to be enriched in multiple IS membrane domains, including the plasma membrane and perinuclear membranes (Fig. 4 A). Fluorescence signal from the plasma membrane of the OS, however, was notably absent.

Curiously, the region of the OS–IS junction appeared to be particularly enriched with the +8 prenyl probes (Fig. 4 A, arrowheads). We wondered if this enrichment indicated that the apical membrane of the IS compartment served as a sink for +8 prenyl proteins, which might be involved in the OS depletion mechanism. The OS–IS junction, however, is a densely packed structure with apical membrane, connecting cilium, calycal processes (CPs), nascent discs, mitochondria, and mature discs (Fig. 2 A), all within a few hundred nanometers. With a resolution limit of ∼240 nm, confocal microscopy does not allow

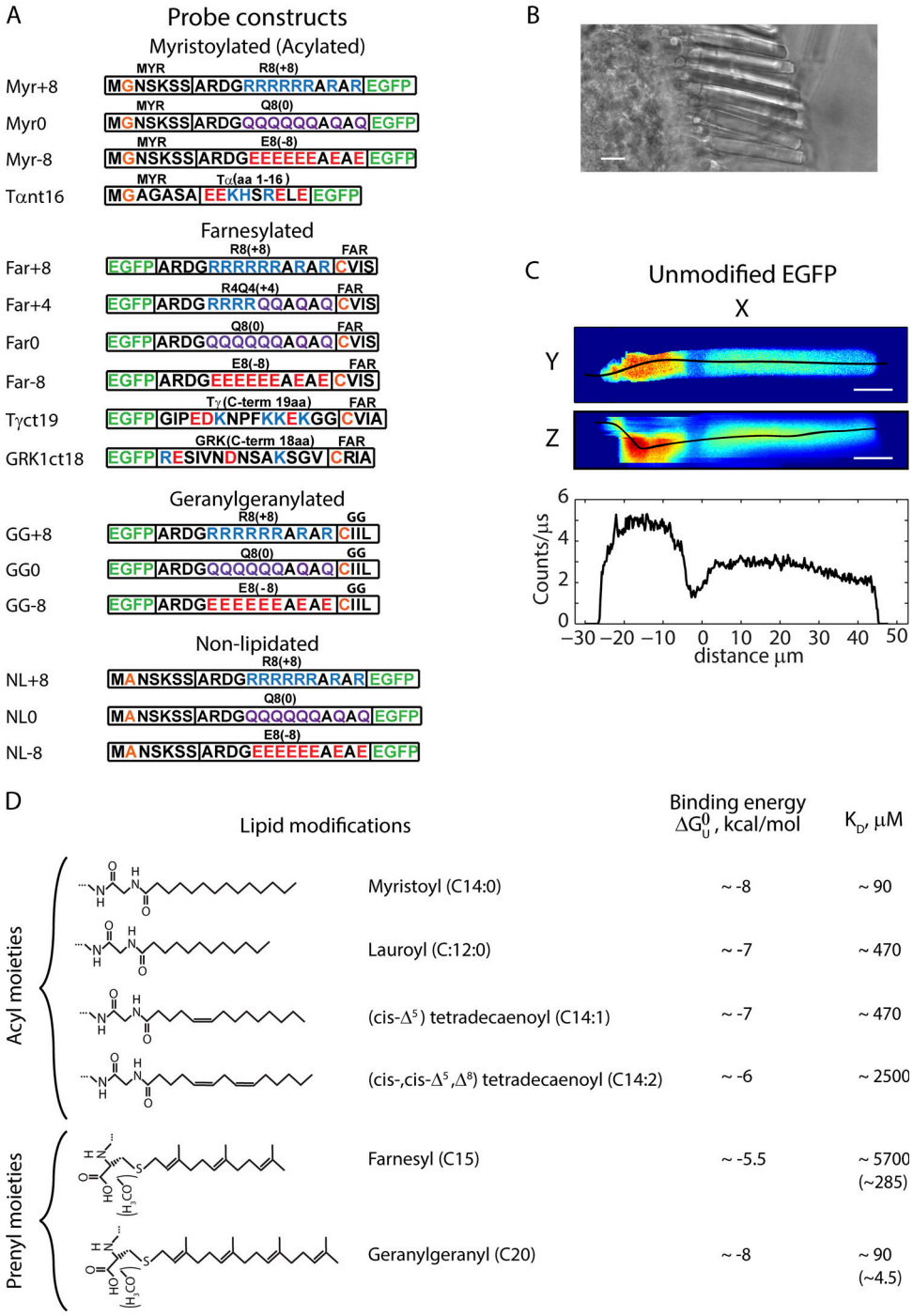

Figure 1. **Expression and quantification of fluorescent probes in rods. (A)** Amino acid sequences of PMP probes. **(B)** Transmission image of retinal slice preparation. **(C)** Confocal image in XY and XZ of a live rod expressing EGFP. Colors are a heat map: red is highest fluorescence, blue is lowest. Axial intensity values (lower panel) were taken along black lines. **(B and C)** Scale bars, 10 µm. **(D)** Structure, name, binding energy, and estimated membrane affinity of the lipid groups. The myristoylation motif results in heterogeneous acylation in retina, with four acyl varieties. In mammalians, the proportions are 55% C14:2, 20% C12:0, 16% C14:1, and 8% C14:0, as determined from mass spec of Tα (Kokame et al., 1992; Neubert et al., 1992; Johnson et al., 1994; Neubert and Hurley, 1998; Lobanova et al., 2007). Throughout, Myr refers to the myristoylation motif and acyl refers to lipids. Two K_ds are given for prenyls, with that for carboxymethylated appearing in parentheses. Binding energies and membrane affinity estimates were based on in vitro partitioning experiments (Peitzsch and McLaughlin, 1993; Silvius and l'Heureux, 1994).

absolute identification of which of these structures contain the probes; however, closer examination gives some important clues.

3D image stacks show that CPs are fluorescent (Fig. 4 B, arrowheads; Videos 1, 2, and 3), an observation bolstered by examining broken OS–IS where some of the CPs are displaced (Fig. 4 C). This shows that some of the OS–IS junction signal comes from the CPs that are contiguous with the apical membrane. To evaluate if the OS–IS junction signal represented a

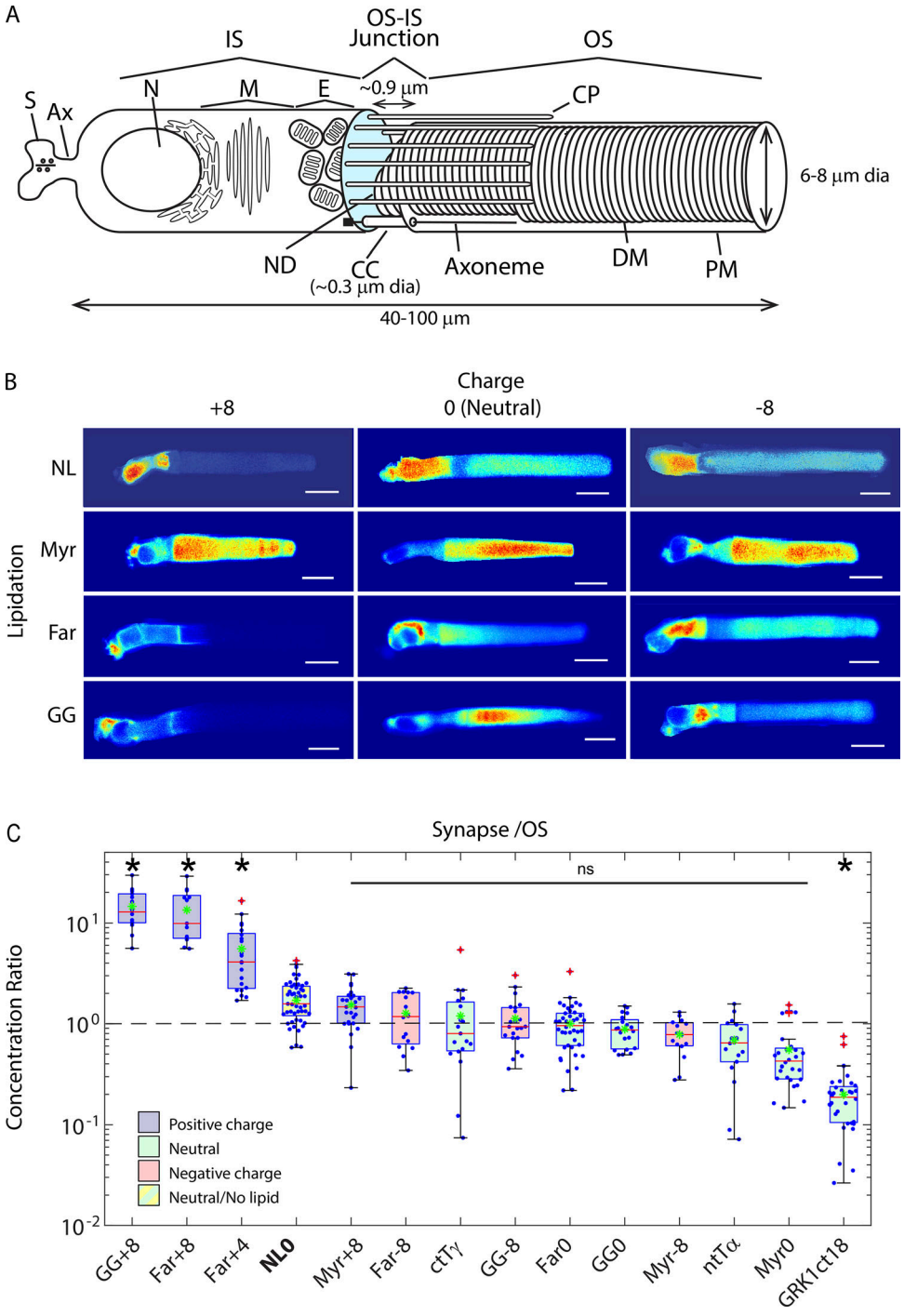

Figure 2. **Lipidation and surface charge, alone, drive compartmentalization of PMPs. (A)** Schematic of amphibian rod. S, Synaptic spherule; Ax, axon; N, nucleus; M, myoid; E, ellipsoid; ND, nascent discs; CC, connecting cilium; DM, mature disc membranes; and PM, plasma membrane. Cyan: Apical membrane. NDs are open to the extracellular milieu and contiguous with the CC and PM. DMs are enclosed within and separate from the OS PM and each other. **(B)** Confocal images of rod cells expressing PMP probes. Scale bars, 10 µm. **(C)** Box-whisker plots of average fluorescence in synapse divided by average fluorescence of OS. In all box-whisker plots, circles represent individual cells, red line is median, box limits are 25th and 75th percentiles, whiskers are interquartile range, excluding outliers (+), and green asterisks are means. Presence of differences among all probes was tested by one-way ANOVA, α = 0.05. Black asterisks indicate significant differences from NL0, determined by Tukey-corrected post hoc two-tailed *t* test. n for each construct: GG+8, 14; Far+8, 13; Far+4, 21; NL0, 29; Myr+8, 27; Far-8, 16; ctTγ, 17; GG-8, 22; Far0, 42; GG0, 20; Myr-8, 15; ntTα, 18; Myr0, 28; and GRK1ct18, 30. ns, not significant.

structure larger than the apical membrane, we analyzed the OS–IS enrichment bandwidth (Fig. 4 D). Intensity profiles of rods expressing Far+8 and GG+8 probes were collected along a computer-generated line that extended axially, through the 3D center of the photoreceptor (Fig. 4 D). On average, the full width at half maximal (FWHM) fluorescence was 726 ± 113 nm for Far+8 and 970 ± 84 nm for GG+8, more than threefold larger than the FWHM of the point spread function (*psf*) intensity

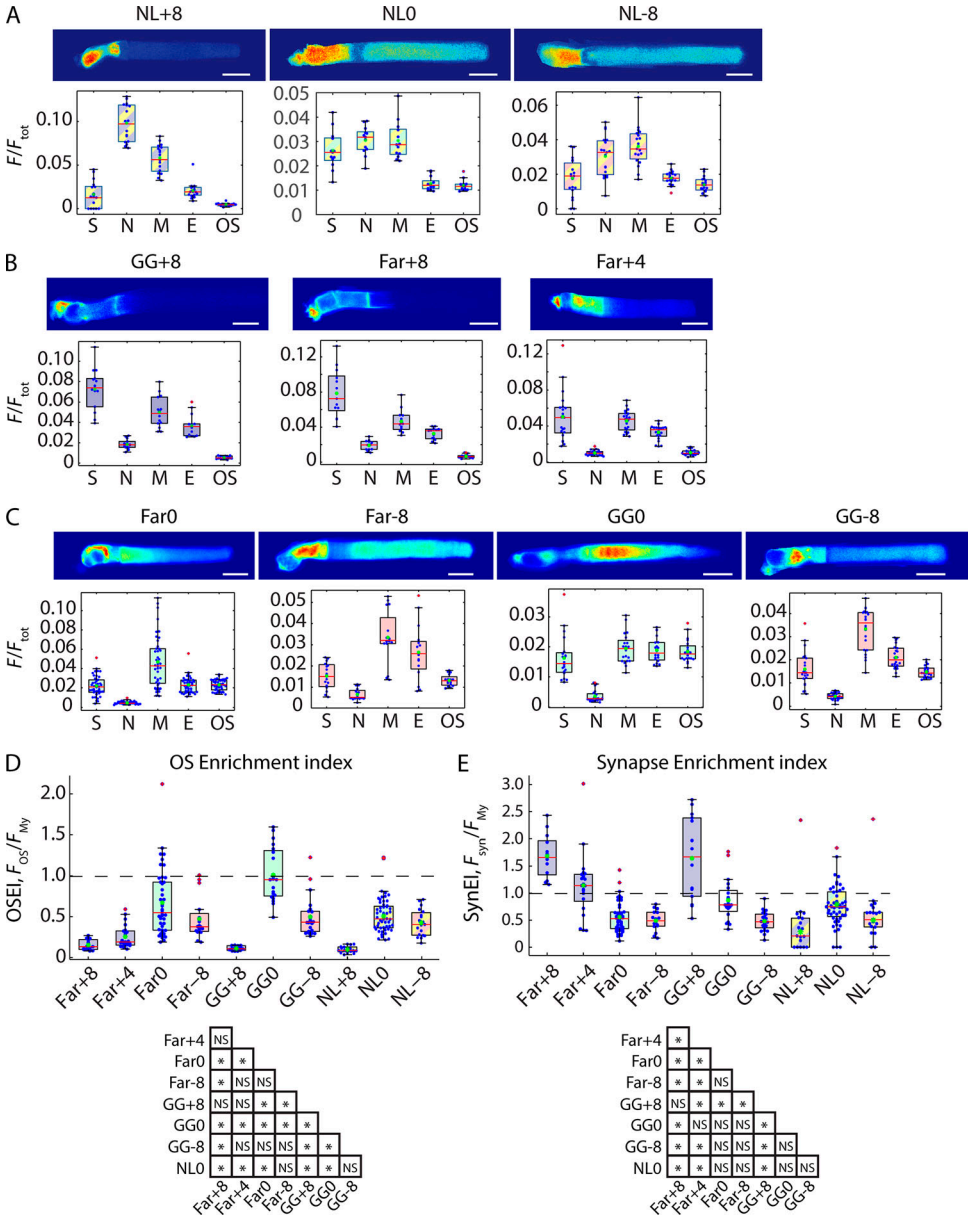

Figure 3. **Distribution of prenylated probes dependds on linker charge. (A–C)** Upper panels, representative confocal images. Scale bars, 10 µm. Lower panels, average compartment fluorescence normalized to total cell fluorescence. **(D)** OSEI, defined as the ratio of average OS fluorescence to average myoid fluorescence, F_{OS}/F_M. **(E)** SynEI, defined as ratio of average synaptic fluorescence to average myoid fluorescence, F_{syn}/F_M. **(D and E)** Lower panels are significance tables. *, P = 0.05; NS, not significant. Box fills as in Fig. 2 C key. Box-whisker plots as described in Fig. 2. n for each construct: NL+8, 14; NL0, 13; NL-8, 17; GG+8, 14; GG0, 20; GG-8, 22; Far+8, 13; Far+4, 21; Far0, 42; and Far-8, 16.

profile, thus showing that the fluorescence signal at the OS–IS junction cannot come from the apical membrane alone.

No structure in the OS–IS junction region, except for the nascent disc membranes that form at the OS base and the fully formed discs enclosed within the OS plasma membrane possess such a flattened shape. Thus, the prenyl +8 probes likely enter the connecting cilium compartment and fill the nascent discs, which extend ∼100–300 nm above the apical membrane (Besharse et al., 1977)—and likely some of the isolated discs within the OS plasma membrane. Further evidence that small amounts of the probe are present in the OS discs comes from analysis of the fluorescence distribution along the full length of the OS (Fig. 4 E). The fluorescence signal is higher proximal to the OS–IS junction and tapers downward along ∼10 µm of the OS (Fig. 4 E, left panels). This pattern is clearly distinct from that of NL0 and other lipidated probes, where the OS distribution is more uniform (Fig. 4 E, right panels).

It was surprising that +8 prenyl probes were enriched in discs at the base of the OS and do not reach more distal discs. Physically, there are few possible mechanistic explanations: +8 prenyl probes either have a nonuniform pattern of relatively high-affinity binding sites in the nascent and basal OS discs, or there is an active mechanism removing the probe from the OS. To distinguish between these possibilities, we examined the mobility of the +8 prenyl probes in the OS–IS junction and

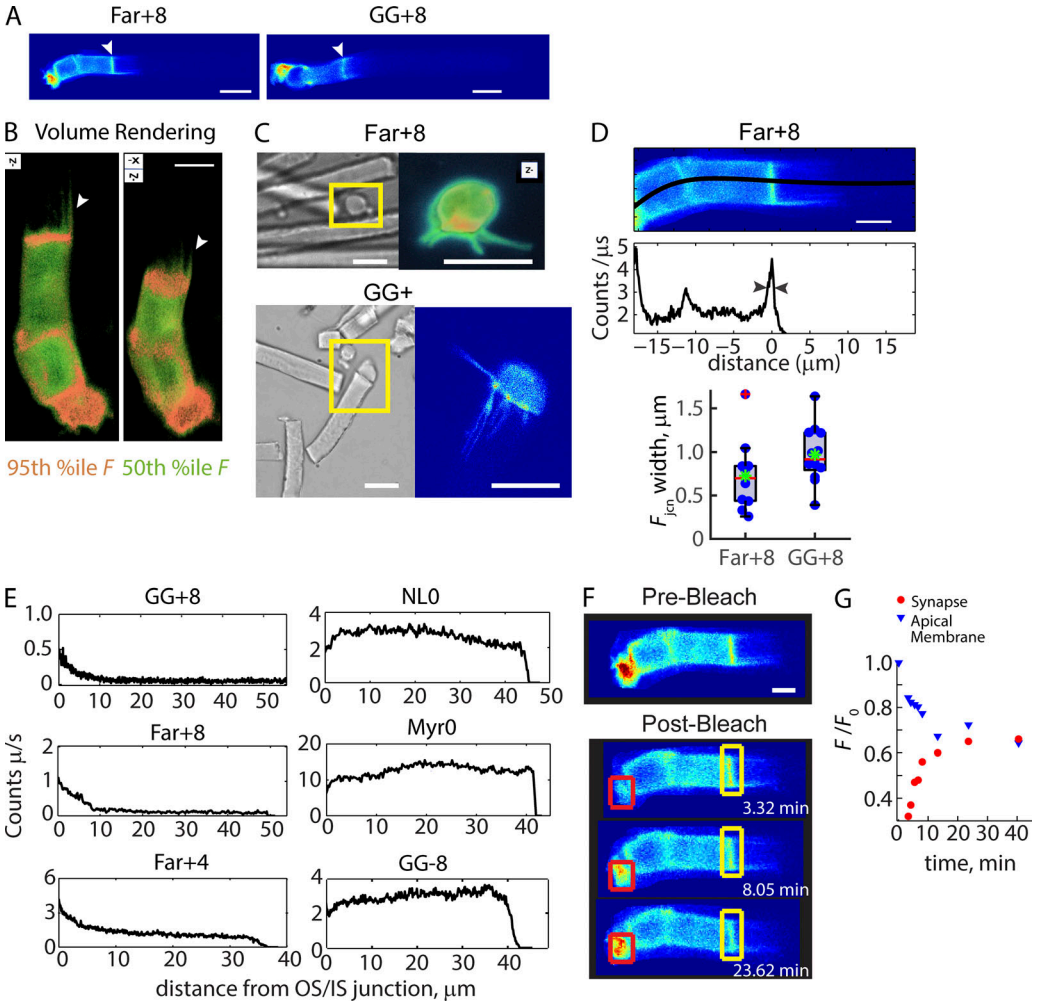

Figure 4. **Positive prenylated probes are enriched in the cell body PM, perinuclear membranes, and the OS–IS junction. (A)** Representative confocal images. Scale bars, 10 µm. Arrowheads: OS–IS junction. **(B)** 3D renderings of the Far+8 rod shown in A, at different angles (see angle indicators). Green: 50th percentile, red: 90th percentile intensities. White arrowheads: CPs (Videos 1, 2, and 3). Scale bar, 5 µm. **(C)** Confocal images of broken OS–IS showing fluorescence-containing CPs separated from OS. Scale bars, 5 µm. **(D)** OS–IS junction enrichment width estimate. Upper panel: Confocal image of Far+8 rod in A with OS–IS junction expanded. Scale bar, 5 µm. Middle panel: Fluorescence intensities as a function of axial distance; zero is the OS–IS junction. Arrowheads show half maximum fluorescence. Bottom panel, Junction widths for Far+8 and GG+8 cells were not different as determined by two-tailed *T* test assuming equal variance. Box-whisker plot as described in Fig. 2. n for each construct: Far+8, 9; and GG+8, 12. **(E)** Fluorescence as a function of distance within the OS. Left panels: Representative profiles from positive prenylated probes. Right panels: OS distributions of other PMPs. **(F)** FRAP of Far+8 in the synapse. Red box: Spherule region of interest (ROI); yellow box: OS–IS junction ROI. Scale bar, 5 µm. **(G)** Time course of synapse fluorescence recovery and OS–IS junction fluorescence loss.

synapse. We reasoned that if the probes were localized to the basal discs due to high-affinity binding, then the probe found in the OS–IS junction would be poorly exchangeable with probe in other regions of the cell body. We found that the synaptic region rapidly recovered after photobleaching, with a $t_{1/2}$ of ~2 min, and that this recovery was mirrored by a decline in signal at the OS–IS junction (Fig. 4, F and G). Thus, Far+8 at the OS–IS junction and the synaptic region are rapidly exchangeable, and binding to these structures is relatively weak.

Distribution and transport of prenylated probes does not require association with the prenyl binding/chaperone protein, PrBPδ

The prenyl binding protein, PrBPδ, has been implicated in the OS transport and localization of PDE6α,β subunits (Zhang et al., 2007; Hanke-Gogokhia et al., 2016; Wright et al., 2016) and GRK1 (Zhang et al., 2007), all of which are prenylated PMPs. We thus explored the possibility that PrBPδ binding to the prenylated probes solubilizes them for transport across the connecting cilium diffusion barrier. A GFP trap assay, however, failed to pull down PrBPδ with any of the engineered prenyl probes examined, despite identifying it in the input and flow-through (Fig. 5, A–C).

We next examined the distribution and PrBPδ association of a probe containing the 18 N-terminal amino acids of GRK1. Interestingly, the OS enrichment index of ~4.5 for EGFP-GRK1ct18 shows that it was highly enriched in the OS compartment (Fig. 5, D and F). The OS enrichment of full-length GRK1 has not previously been determined. However, our analysis of immunohistochemical staining of GRK1 in mammalian photoreceptors

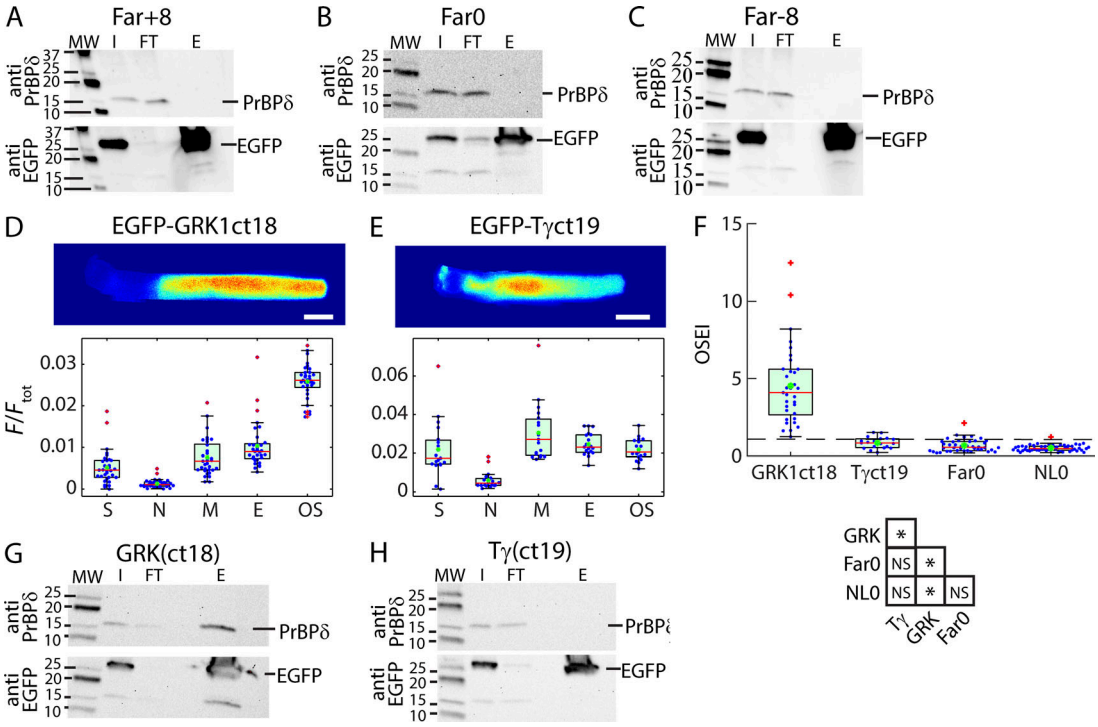

Figure 5. **Prenylated PMP transport to OS does not require association with LBC protein, PrBPδ. (A–C)** GFP trap of prenylated probes fail to pull down PrBPδ. Western blots probed with anti PrBPδ antibody. **(D and E)** Upper panels: Representative confocal images of GRK1 and Tγ probes. Scale bars, 10 µm. Lower panels: Normalized compartment distributions. **(F)** OSEIs showing higher OS enrichment of GRK1. Significance table: P ≤ 0.05; NS, not significant. **(G and H)** GFP trap of GRK1 and Tγ probes show that GRK1ct18 associates with PrBPδ while Tγct15 does not. Box-whisker plots as described in Fig. 2. n for each construct: GRK1ct18, 30; Tγct19, 17; Far0, 42; and NL0, 29. **(A–C, G, and H)** MW, molecular weight markers; I, input; FT, flow through; and E, eluate.

(Zhao et al., 1998; Grossman et al., 2011; Osawa et al., 2011) showed a range of two to four for the OSEI, in reasonable agreement with the enrichment of EGFP-GRK1ct18. Our results thus show that the N-terminal 18 amino acids of GRK1 are sufficient to encode GRK1 OS enrichment.

GFP trap of EGFP-GRK1ct18 quantitatively pulled down endogenous *X. laevis* homologue of PrBPδ (Fig. 5 G). In contrast, a farnesylated probe containing the 19 N-terminal amino acids of transducin γ, EGFP-Tγct19, like the other engineered Far probes, failed to pull down endogenous PrBPδ (Fig. 5, A–C and H), and its distribution was not different from NL0 (Fig. 5, E and F), in agreement with previous reports in PrBPδ knockout mouse (Zhang et al., 2007). These results directly show that PrBPδ interaction with GRK1 is necessary for its OS enrichment. However, PrBPδ is not necessary for prenylated proteins to gain access to the ciliary OS compartment.

Acylation leads to probe enrichment within the OS independent of linker charge or association with Unc119

We next examined the enrichment of acylated probes in the OS and synapse compartments relative to the myoid (Fig. 6). All Myr probes were significantly enriched in the OS, relative to NL0, regardless of linker charge (Fig. 6, A and C). Myr0 had the highest OSEI at 2, and Myr+8 and Myr-8 were approximately equally OS enriched with OSEI ∼1; NL0 OSEI was 0.45 (compare Fig. 3, A and D). The distribution of nt16Tα-EGFP was not significantly different from Myr+8 or Myr-8 (Fig. 6, B and C). Myr0 had a significantly higher OSEI than Myr+8, Myr-8, and nt16Tα-EGFP (Fig. 6 C).

Except for Myr+8, the SynEIs for all Myr probes was ∼0.75, not different from NL0 (Fig. 6 D). At ∼1.6, Myr+8 SynEI was significantly higher, showing that positive charge on a myristoylated PMP can lead to synapse enrichment. However, none showed significant preference between the major rod compartments (OS and synapse; Fig. 2 C). This result shows that in order for myristoylated PMPs to be enriched in one or other of the major functional compartments, an active process of enrichment or depletion of probe would be required, as observed with the prenyl probes.

Previous studies have implicated an acyl binding protein, uncoordinated 119 (Unc119), in the transport and OS enrichment of Tα (Zhang et al., 2011). We were somewhat surprised that the nt16Tα probe was not enriched in the OS beyond the generic Myr probes (Fig. 6, B and C). Thus, we wondered whether the Unc119 mechanism was operating in frog rods. A search of Xenbase showed that the *X. laevis* genome possesses two homologues, one to Unc119 and the other to Unc119b (Xenbase gene IDs: XB-GENE-6487917 and XB-GENE-17343734, respectively), with ∼80% homology to mouse Unc119. However, Western blots of *X. laevis* retina extract with three Unc119 antibodies failed to identify xUnc119, showing that either it was not expressed in retina or the antibodies did not cross-react. To distinguish between these possibilities, we performed mass spectrometry protein identification on the 25–30 kD MW region of retinal

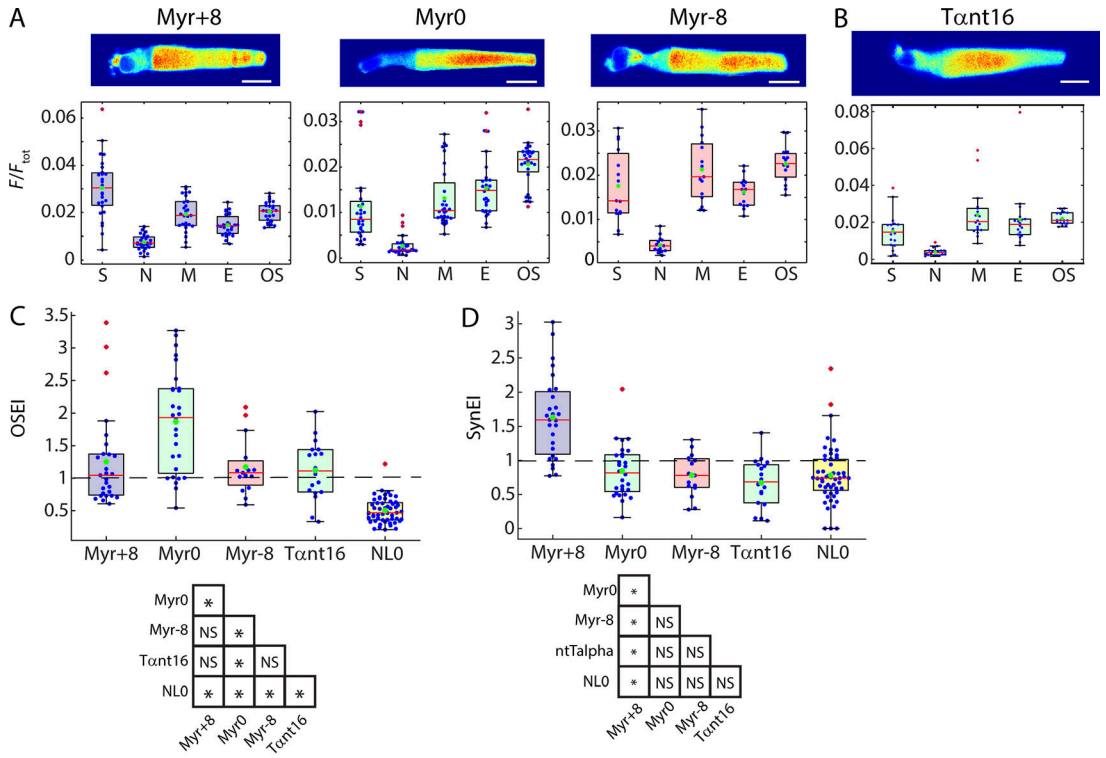

Figure 6. **Myristoylated probes are enriched in the OS regardless of linker charge. (A)** Upper panels: Representative confocal images of rods expressing Myr probes. Lower panels: Compartment distribution profiles. **(B)** Confocal image and compartment distribution profile of Tαnt16. **(A and B)** Scale bars, 10 µm. **(C)** OSEIs of myristoylated probes. Box-whisker plots as described in Fig. 2. Significance table shows that all probes had significantly higher OSEIs than NL0. **(D)** SynEIs show that Myr+8 is the only presynapse enriched probe. Significance tables: $P \leq 0.05$; NS, not significant. n for each construct: Myr+8, 27; Myr0, 28; Myr-8, 15; and Tαnt16, 18.

extract run on SDS PAGE. xUnc119 was identified in this band, showing that it is indeed expressed in *X. laevis* retina (Table S1).

We examined GFP trap pulldowns of probes with mass spectrometry protein identification. GFP trap from retinas expressing Myr0-EGFP failed to pull down xUnc119 (Table S2), while xUnc119 was identified in nt16Tα-EGFP pulldowns (Table S3). Thus, Myr0 probe was not a significant binding partner for Unc119. Importantly, the mass spec analysis of the Myr0-EGFP probe GFP trap eluate contained ∼1,500 different proteins, from virtually every membrane compartment, including synaptic vesicles, IS plasma membrane, OS plasma membrane, mitochondria, lysosomes, and disc membranes. Despite this rich trove of proteins, no other known or putative LBC proteins were identified (Table S2). Thus, acylated probes enter and become enriched within the OS without Unc119 interactions, in agreement with Unc119 knockout studies in mice (Zhang et al., 2011), and without interactions with other LBCs. Moreover, the lack of OS localization of the nt16Tα-EGFP probe directly shows that Unc119 association alone is not sufficient for strong OS enrichment of Tα.

Binding affinity to disc membranes is not sufficient for localizing PMPs to the OS

Extant models for ciliary enrichment of lipidated PMPs suggest that LBC proteins solubilize the PMPs, allowing them to diffuse in the cytoplasm between ER/Golgi and carrier vesicles, or to diffuse directly into the ciliary compartment, where they are then released onto the vesicle or disc membranes (Hanke-Gogokhia et al., 2016; Wright et al., 2016). These models assume that the PMPs tightly bind to target membranes and that the localization is the result of local binding sinks. While such mechanisms are consistent with LBC knockout experiments (Zhang et al., 2007; Hanke-Gogokhia et al., 2016; Wright et al., 2016), the central premise of the mechanism, tight membrane binding, has not been directly tested. We reasoned that because the rod OS disc membranes are isolated from the plasma membrane, and from each other, the mobility along the length of the OS compartment would be a direct measure of the affinity of the probe for disc membrane. Thus, to test the idea, one need only examine the mobility of the probes along the OS compartment length and compare them to the mobility of unmodified E/PAGFP. The geometry of the OS makes it an ideal, and perhaps the only in vivo model for assessing the ciliary membrane affinity of PMPs.

PAGFP or EGFP probes expressed in rods were photoactivated or photobleached in patches of arbitrary size along the OS length, and the redistribution was followed over time (Fig. 7, A and B). To quantify the mobilities of the probes, we fitted the relaxation time courses to a bounded diffusion model (Theory, see Calvert et al., 2010). Diffusion coefficients along the length of the OS, D_{OS}, were estimated by root mean square error minimization (Fig. 7, B and C). Surprisingly, D_{OS} of GRKct15-EGFP

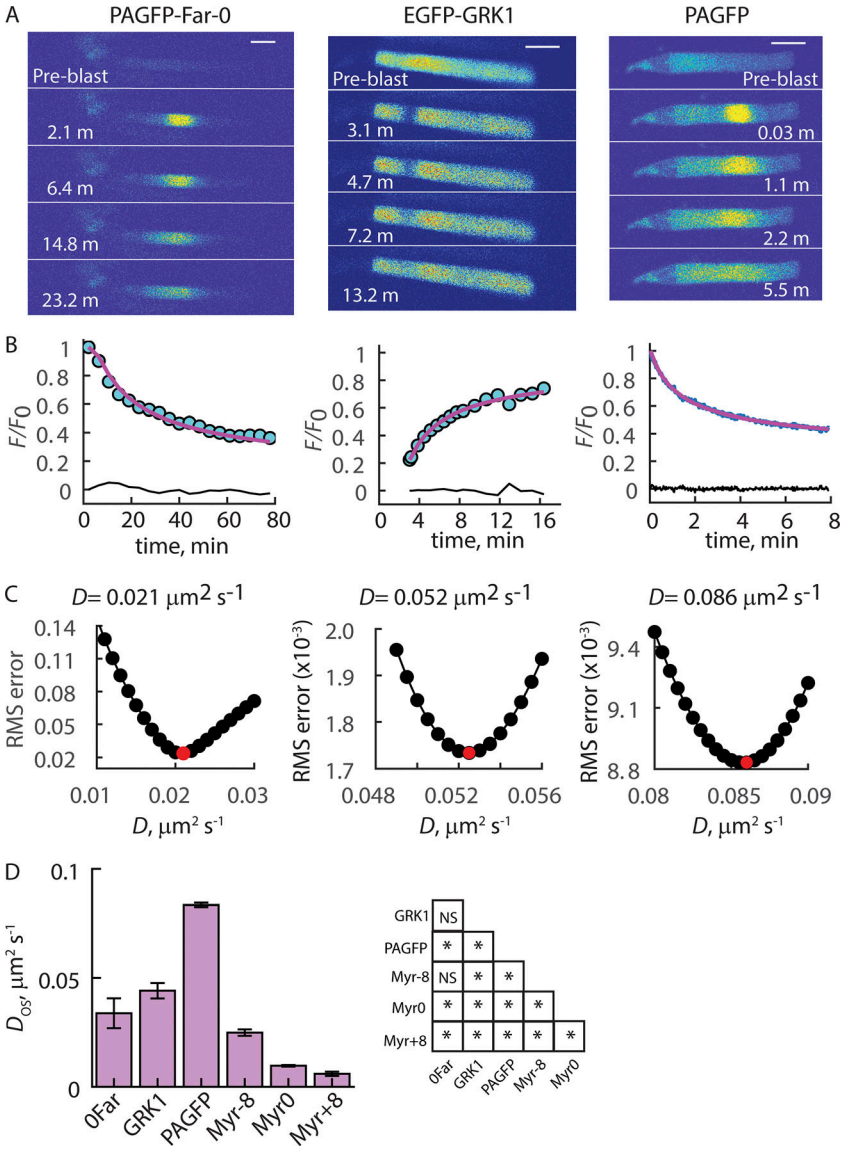

Figure 7. **OS mobility shows low affinity binding of prenylated probes to disc membranes and that binding affinity of myristoylated probes scales with charge. (A)** Representative time course images of FRAPa or FRAPb experiments. Pre-blast images: Distributions before two-photon photoactivation or photobleaching. Scale bars, 10 µm. **(B)** Time courses of fluorescence relaxation at the center of the photoconversion sites fitted with a 3D cylindrical diffusion model, magenta lines. Black lines: Data-model difference. **(C)** Root-mean-square (RMS) errors plotted against *D*. red circle indicates *D* with lowest error, and value shown above plots. **(D)** Bar chart of average D_{OS}s. Error bars are SEM. ANOVA followed by two-tailed, homoscedastic *t* test with Tukey correction showed that D_{OS}s for all lipidated probes were significantly different from the D_{OS} for PAGFP. D_{OS}s among 0Far and GRK1 were not different. Significance tables: P ≤ 0.05; NS, not significant. n for each construct: 0Far, 6; GRK1, 5; PAGFP, 6; Myr-8, 8; Myr0, 3; and Myr+8, 3.

was not significantly different from that of Far0, and only approximately twofold lower than unmodified E/PAGFP (Fig. 7 D). Thus, GRKct15 binds to disc membranes with approximately the same low affinity as Far0, a probe that does not localize to the OS.

The affinity of Myr probes for the OS disc membranes differed up to fourfold depending on linker charge, with the Myr8+ having the highest affinity, and thus the lowest D_{OS}, and Myr8– the lowest affinity and the highest D_{OS} (Fig. 7 D). The OSEI did not, however, follow the disc affinities of the probes. Myr0 was significantly more OS enriched than either Myr+8 or Myr-8, which were enriched to approximately the same extent. Thus, OS enrichment of acylated probes did not appear to result from affinity to disc membranes.

Previous studies in mammals have shown that the myristoylation motif found on Tα leads to heterogeneous acylation (mostly C14:2 and C14:1/C12:0) (Kokame et al., 1992; Neubert et al., 1992; Johnson et al., 1994; Neubert and Hurley, 1998; Lobanova et al., 2007), although in frogs Tα possessed C14:2 only. Among these lipids, C14:2 has the lowest affinity for membranes, on par with that of Far0 (Peitzsch and McLaughlin, 1993; Silvius and l'Heureux, 1994). C14:1 and C12:0 have equal, approximately fivefold higher affinity than C12:2. The affinity of C14:0 is fivefold higher again. D_{OS} for Myr0 in our study was approximately four- to fivefold lower than that of Far0 (Fig. 7 D), and the relaxation of the photoconversion field in FRAP experiments was well fitted assuming a single diffusion coefficient. Thus, the Myr probes in our study were predominantly modified with C14:1 and/or C12:0 acyl lipids.

The connecting cilium is a leaky barrier to PMP diffusion

An alternative to the tight binding sink mechanism for retaining PMPs in the OS may be restriction of movement through the connecting cilium by means of a diffusion barrier. Diffusion barriers for intrinsic membrane and soluble proteins at cilia transition zones have been proposed by several groups (Sorokin, 1962; Spencer et al., 1988; Vieira et al., 2006; Geneva and Calvert,

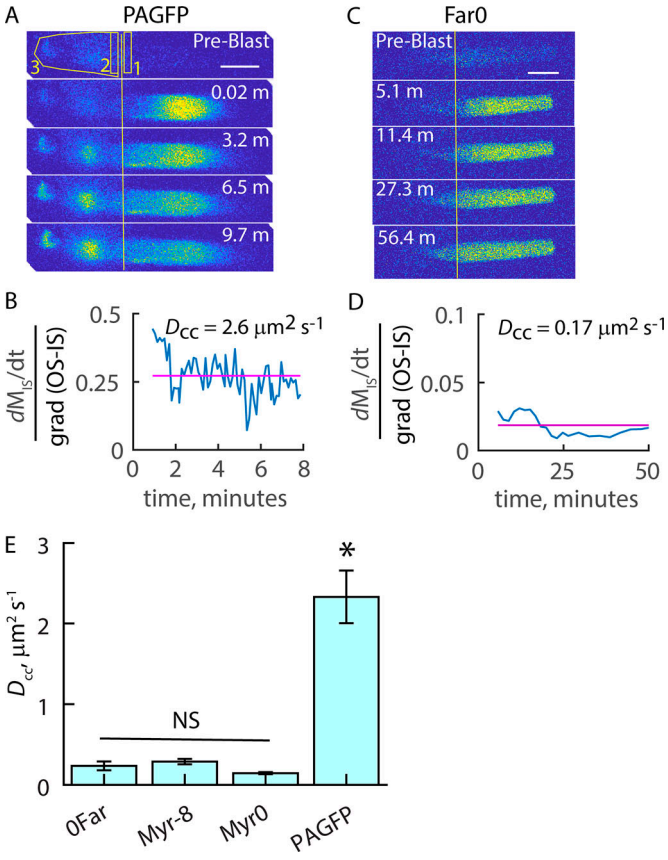

Figure 8. **Lipidated probes move through the connecting cilium via impeded diffusion. (A and C)** Time course images of PAGFP or Far0-PAGFP flux into the IS. Vertical lines indicate the OS–IS junction. At time zero, PAGFP was activated by two photon scanning over 70–80% of the OS. ROIs were drawn to find c_{OS} (ROI1), c_{IS} (ROI2); and M_{IS} (ROI3; Eq. 1). Scale bars, 10 µm. **(B and D)** Flux normalized to OS–IS concentration gradient (grad [OS-IS]). Line is linear regression. D_{CC} was estimated according to Eq. 1. **(E)** Average D_{CC}s; error bars: SEM. Asterisk indicates D_{CC} of PAGFP was significantly higher than those of the lipidated probes at P = 0.05, as determined by two-tailed *t* test.

2010; Hu et al., 2010; Kee et al., 2012; Endicott and Brueckner, 2018). Although we have previously demonstrated that soluble proteins up to ∼80 kD can pass through the rod connecting cilium (Najafi et al., 2012) and it was later shown that the transition zone of primary cilia appears permeable to proteins up to ∼80 kD (Breslow et al., 2013), the permeability of PMPs through the cilium base has not been previously examined. We thus quantified PMP transport through the connecting cilium using analysis of ciliary protein flux (Calvert et al., 2010; Fig. 8). PAGFP probes expressed in rods were photoactivated within the ciliary OS, and their equilibration throughout the rod was monitored over time (Fig. 8, A and C). The flux of protein through the connecting cilium was measured and normalized to the concentration gradient of the photoconverted molecules from the OS to the cell body. This approach allows a direct estimation of the diffusion coefficient through the connecting cilium as follows.

Rearrangement of Fick's first law yields a normalized flux term, *nFlux*,

$$\frac{dM_{IS}/dt}{[c_{OS}(t) - c_{IS}(t)]} = nFlux = D_{CC}\frac{A_{cc}}{l_{CC}}, \quad (1)$$

where dM_{IS}/dt is the flux of molecules from the OS, through the connecting cilium and into the IS, $[c_{OS}(t) - c_{IS}(t)]$ is the time varying concentration gradient, D_{CC} is the effective diffusion coefficient through the connecting cilium for the molecular species, and $\frac{A_{cc}}{l_{CC}}$ is the ratio of the area of cross-section, A_{cc} and the length of the connecting cilium, l_{cc}. *nFlux* is time invariant if transport is via simple diffusion. The magnitude of D_{CC} may then be obtained based on measured *nFlux* and estimates of A_{CC} and l_{CC} from published EM studies (Calvert et al., 2010). The entire cross-section of the CC is used in A_{CC} estimation, so the effective D_{CC} reflects any tortuosity, other properties of the axoneme, or other ciliary contents that may impact free diffusion.

nFlux was time invariant for all of the engineered lipidated probes we analyzed (Fig. 8 D), showing that their transport through the connecting cilium was via simple diffusion. D_{CC} of PAGFP-0Far, Myr-8-PAGFP, and Myr0-PAGFP were 10-fold lower than that of unmodified PAGFP (Fig. 8 E), indicating that the permeability of the connecting cilium to the lipidated probes was significantly lower than that of the unmodified PAGFP. This difference cannot be attributed to binding of probes to OS disc membranes alone since D_{OS} of Far0 and Myr-8 were only approximately twofold lower than that of PAGFP (Fig. 7). Note that the D_{OS} was invariably lower than D_{CC} for all probes measured. This is due to the high degree of tortuosity of the diffusion paths imposed by the disc membranes (Calvert et al., 2010). Thus, the connecting cilium impedes but does not prevent the intercompartment diffusion of lipidated proteins.

Diffusion-binding-active transport (DBT) model of subcellular enrichment of PMPs

Thus far our results have revealed that lipidated proteins have varied affinities for disc membranes, their transport through the connecting cilium is impeded, and their distributions depend on both the lipid moiety and linker charge. How these factors come together to produce the various steady-state distributions, however, is not clear. In this section we use a DBT model to explore the impact of measured parameters on the steady-state distributions of PMPs.

The DBT model (Eq. 2; and Theory Eqs. A13, A14, and A15) allows computational evaluation of the impact of spatially variable diffusivity, local binding, and local active transport on the dynamics and steady-state distributions of molecules in polarized cells.

$$\frac{\partial c_f}{\partial t} = \frac{1}{\left[1 + \frac{B(z)K_d(z)}{(K_d(z) + c_f)^2}\right]}\frac{1}{A(z)}\frac{\partial}{\partial z}\left(A(z)D(z)\frac{\partial c_f}{\partial z}\right) - \frac{1}{A(z)}\frac{\partial(A(z)v(z)c_f)}{\partial z}. \quad (2)$$

Eq. 2 consists of three terms representing local binding,

Table 1. **DBT model variables and units**

Variables	Description	Units
c_f	Concentration of unbound molecules	M
B	Maximum binding capacity	Moles per unit area of membrane
K_d	Dissociation constant	M
A	Area of cross section	μm^2
D	Axial diffusion coefficient	$\mu m^2 s^{-1}$
v	Transport velocity	$\mu m\ s^{-1}$

$$1 \Big/ \left[1 + \frac{B(z)K_d(z)}{\left(K_d(z) + c_f\right)^2}\right],$$

diffusion,

$$\frac{1}{A(z)} \frac{\partial}{\partial z}\left(A(z)D(z)\frac{\partial c_f}{\partial z}\right),$$

and active transport,

$$\frac{1}{A(z)} \frac{\partial\left(A(z)v(z)c_f\right)}{\partial z}.$$

To reduce computational burden, we assume that the cell is approximately cylindrical and that transport of molecules along the shorter radius of the cell is fast relative to transport along the longer axis (see rod schematic, Fig. 2 A). This allows reduction of the model to a single spatial dimension, except that the area of cross-section varies with distance. To account for this, an axially variable area of cross-section, $A(z)$, was introduced. As the binding term shows, local binding is assumed to operate according to a Langmuir isotherm. The synaptic spherule and distal tip of the OS are treated as no-flux boundaries (Theory Eq. A14), i.e., molecules cannot leave the cell. Finally, we assume the concentrations of molecules remain constant over the time required for equilibrium distribution to be achieved, i.e., no molecules are being synthesized or degraded. Model variables and their units are given in Table 1.

We used the model to examine EGFP-Far0 and EGFP-GRK1ct18 probes because of the striking difference in their steady-state distributions despite similar D_{OS} and linker charge. The major difference between these probes is that EGFP-GRK1ct18 binds with PrBPδ, whereas EGFP-Far0 does not. PrBPδ has been shown to distribute throughout the cell body, but was absent from the rod OS in frog rods (Norton et al., 2005). The modest reduction of the D_{OS} from E/PAGFP suggests the membrane binding affinity is low for these probes, but how low binding affinity, particularly if it is not spatially uniform, impacts distribution is not clear. We thus initially explored if modest affinity binding in the OS, relative to the cell body, could lead to the OS enrichment observed for EGFP-GRK1ct18 (Fig. 9, A–C).

We estimated the binding affinities of the probes by finding the capacity, B, and the dissociation constant, K_d, in the diffusion-binding model that reduced the apparent OS diffusion coefficient twofold. We then introduced the observed 10-fold diffusion impediment to PMPs traversing the connecting cilium in the full DBT model and allowed it to run until a steady-state distribution was achieved. We found that a variety of combinations of K_d and B could produce the twofold changes in the effective D_{OS} with similar changes in OSEI; thus, we present the results in terms of equivalent binding power (EBP), where EBP ≈ K_d/B. An EBP of 1.5 resulted in twofold reduction in effective D_{OS} but produced an OSEI of only ∼0.55, slightly higher than unmodified E/PAGFP but not close to the OSEI of approximately five observed for EGFP-GRK1ct18 (Fig. 9, B, C, and F). Higher OSEI were obtainable with higher affinity OS binding, but at the cost of dramatically reduced OS mobility (Fig. 9 F).

Introducing active transport within the connecting cilium with an OS-directed transport velocity, $v \approx 0.55\ \mu m\ s^{-1}$ combined with the weak OS binding resulted in OSEI of ∼0.8 (Fig. 9, D and F). To put this velocity into perspective, given that GRK1 is present in the rod at a ratio of 1:800 rhodopsins (Klenchin et al., 1995), which corresponds to a cytoplasmic concentration of ∼3.75 μM, $v = 0.55\ \mu m\ s^{-1}$ is equivalent to transporting ∼17 molecules of GRK1 per second through the axoneme-excluded CC. Finally, adding a CC diffusion impediment, reducing D_{cc} to $0.4\ \mu m^2\ s^{-1}$, was necessary to achieve the OSEI of approximately five (Fig. 9, E–G). Active transport of some form and impeded connecting cilium diffusion thus appear to be the major factors needed to produce the observed OS enrichment of EGFP-GRK1ct18, and by extension, enrichment of GRK1.

Finally, we examined whether a weak local binding sink could account for the degree of synapse enrichment and the rapid exchange among IS pools found for Far+8 (Fig. 9, H–J). Indeed, a K_d of 0.5 μM in the synapse was sufficient to produce the observed SynEI, with a $t_{1/2}$ of FRAPb recovery of ∼2 min, as observed for Far+8.

Discussion

Extant models for the transport and confinement of PMPs to subcellular compartments include vesicular transport, transport by motor-driven protein complexes, and diffusion, all of which are mediated by LBC proteins (Baehr, 2014; Jensen and Leroux, 2017). All of these theories involve tight membrane binding or a selective diffusion barrier to maintain steep concentration gradients, i.e., they either implicitly or explicitly hypothesize that once a PMP is delivered to a compartment, it remains there indefinitely.

Our results do not fit this model. Weak membrane binding of PMPs in our study shows that they would not remain on their target membranes for more than a few minutes. The DBT model predicted that moderate binding within the synaptic spherule could lead to significant synapse enrichment, while maintaining rapid exchangeability with other cell body membranes. However, neither the weak binding to disc membranes nor the modest impediment to diffusion imparted by the connecting cilium could explain PMP enrichment within the ciliary OS.

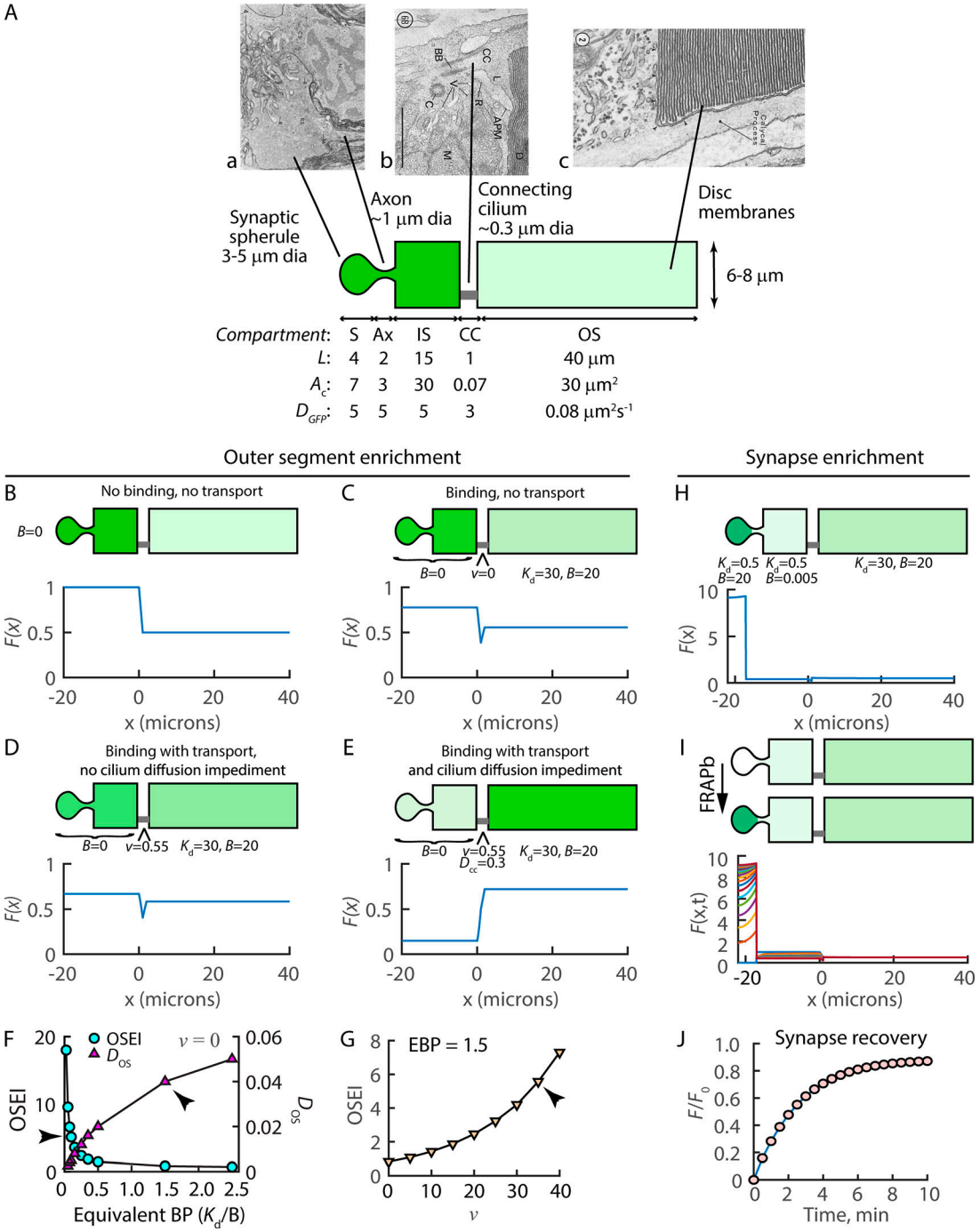

Figure 9. **Contributions of local binding, active transport, and cilium diffusion impediment to OS and synaptic enrichment of PMPs, computed by the DBT model. (A)** Schematic of model rod with compartments labeled as in Fig. 2 A. Representative electron micrographs show the geometries of the compartments. Note the many synaptic vesicles filling the spherule (a) and the density and order of OS disc membranes (c). Parameters for each compartment used in all computations are listed: *L*, length; A_c, area of cross-section; and D_{GFP}, diffusion coefficient of unmodified EGFP. EM images reproduced with permission from a (Schacher et al., 1976), b (Peters et al., 1983), and c (Townes-Anderson et al., 1985). a and b, Scale bars, 1 μm. c, Magnification = 45,000. dia, diameter. **(B–E)** DBT predictions of EGFP-GRK1ct18 distribution show that active transport and the connecting cilium diffusion impediment, together, are the major contributors to OS enrichment; local OS binding played a minor role. **(F)** Predictions of OSEI, *F*(OS)/*F*(IS) from model traces, and effective D_{OS}, found by fitting model FRAPs as described in Fig 7, plotted versus equivalent binding power. Arrowhead on the D_{OS} line shows that at EBP = 1.5, D_{OS} was approximately twofold lower than that for no binding, as found experimentally for EGFP-GRK1ct18 and EGFP-Far0 versus EGFP (Fig. 7). However, the OSEI was <1. The OSEI line shows that tighter OS binding can lead to fivefold (arrowhead) or better OS enrichment, but at the cost of mobility. BP, binding power. **(G)** Transport velocity versus predicted OSEI, given OS EBP = 1.5. Arrowhead indicates the velocity that produces the observed approximately fivefold OS enrichment, as found experimentally for EGFP-GRK1ct18. **(H–J)** Higher synapse affinity resulted in significant enrichment (H) and FRAP recovery $t_{1/2}$ ~2 min (I and J), similar to experimental results for Far0 (Fig. 4 G), suggesting the distribution of Far0 within the IS is mediated by equilibrium binding alone.

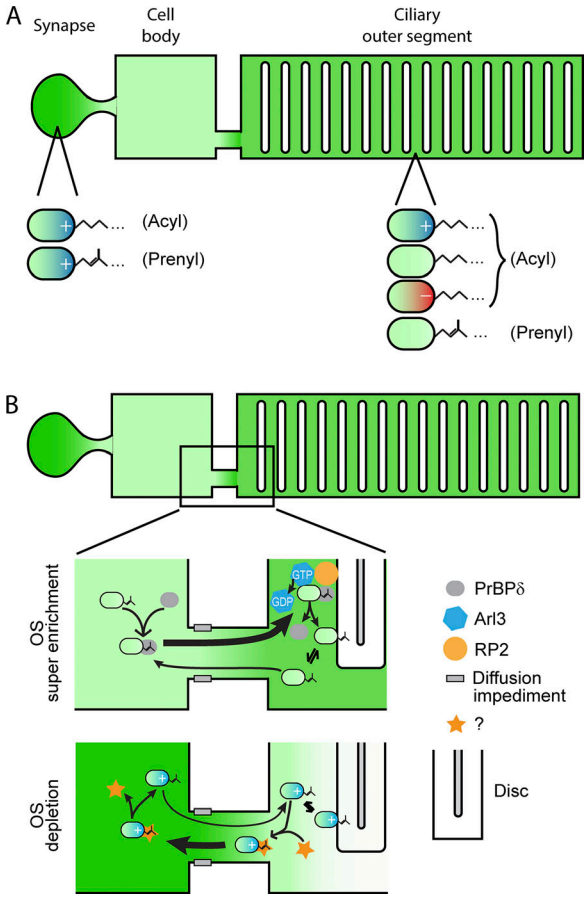

Figure 10. **The photoreceptor PMP compartmentalization code.** In the absence of interactions with chaperones, PMPs tend to distribute according to a few simple rules. Positive charge near any lipid moiety leads to synaptic enrichment. Myristoylated proteins with any charge and neutral prenylated proteins slightly favor the ciliary OS. All others are distributed like unmodified EGFP (A). To achieve "super" enrichment of the OS or synapse compartments, active mechanisms to enrich or deplete the ciliary OS must come into play (B).

A novel model for PMP enrichment within, and depletion from the ciliary rod OS: Continuous ciliary recycling

Fig. 10 summarizes our findings and provides an alternative model for PMP enrichment in rod compartments. PMPs appear to distribute based on variations in local, weak membrane affinity, which can lead to modest enrichment in the synapse or OS (Fig. 10 A). To achieve higher degrees of enrichment ("super enrichment"), the DBT model shows that the weak membrane binding and a leaky connecting cilium can be overcome by continuous recycling of proteins into or out of the OS (Fig. 10 B). At steady-state, an IS to OS transport rate of ∼17 proteins per second was sufficient to maintain the observed OSEI of approximately five for EGFP-GRK1ct18. This is a modest rate of protein transport when compared with the ∼3,500 rhodopsins per second that is required to replenish 10% loss of the OSs to daily disc shedding (Besharse et al., 1977; Hollyfield et al., 1977). One wonders, however, if the continual recycling mechanism represents a significantly higher metabolic burden than would be the case for one-way delivery and permanent attachment of newly synthesized GRK1s to nascent discs. To address this question, we approximated the delivery load for the one-way mechanism to be 4.3 GRK1s per second, based on turnover of 10% of the OS per day and GRK1 expressed at 1:800 rhodopsins, approximately fourfold fewer than needed for the continual recycling mechanism. Assuming either mechanism requires hydrolysis of one GTP per GRK1 delivered, recycling was only slightly more energetically costly. Factoring in the energy needed to synthesize new GRK1s likely makes recycling more efficient than the one-way mechanism.

There are advantages to weak disc membrane binding. It allows equilibration throughout the OS, ensuring uniform activity of the PMPs. It may also allow more rapid turnover of the PMPs. At steady-state, delivery of 17 GRK1s per second into the OS is balanced by 17 leaking back out. If half of the 17 molecules were replaced, the entire complement of GRK1s could be turned over in ∼5 d, rather than the 6 wk required for turnover of the OS in frogs (Besharse et al., 1977; Hollyfield et al., 1977).

Depletion of PMPs from the OS, required for super enrichment of the synapse, may operate through a similar, IS-directed continuous recycling mechanism. Our results suggest prenyl+8 probes diffuse through the connecting cilium and into the OS, but are then continuously removed from the ciliary compartment. Recent studies have reached similar conclusions for intrinsic membrane proteins in rods and cells possessing primary cilia (Datta et al., 2015; Ye et al., 2018).

The connecting cilium operates as an active PMP sorting platform

The results suggest the connecting cilium, equivalent to the ciliary transition zone, is an active sorting platform for compartment enrichment. Transport into the OS may operate through an anisotropic diffusion mechanism like that proposed for transport of soluble proteins through the nuclear pore complex (Kee et al., 2012; Jovanovic-Talisman and Zilman, 2017), but imparted by lipid binding chaperone proteins. For example, PrBPδ-associated GRK1 may pass through the connecting cilium into the OS without encountering the diffusion impediment and then be released by Arl3/Arl13b and the OS localized RP2 (Baehr, 2014; Hilgendorf et al., 2016). Once inside the OS, GRK1 would be in a rapid binding and dissociation cycle with disc membranes, allowing it to equilibrate easily along the OS, but also to diffuse back into the cell body (Fig. 10 B). In the OS to IS direction, a possible mechanism for depleting PMPs from the OS could be removal by the Bardet-Biedl transport complex, the BBSome, which has recently been implicated in removal of membrane proteins from photoreceptor OSs and primary cilia (Datta et al., 2015; Ye et al., 2018). Further study is required to determine how PMPs are sorted at the connecting cilium and ciliary transition zone.

Another mechanism that may drive enrichment of charged proteins across the connecting cilium and within the major rod compartments is voltage gradient–induced electrophoresis. Hagins et al. (1970) showed that the circulating current in dark-adapted rods would produce a significant cytoplasmic potential gradient along the rod axis, with the tip of the OS being positive

relative to the rod base and IS. This potential difference would produce an electrophoretic driving force on charged molecules, with negatively charged molecules driven toward the OS tip and positively charged molecules driven toward the OS base and into the cell body. The depletion of the NL+8 probe from the OS (Fig. 3 A) suggests electrophoretic enrichment may be an important factor in setting charged protein distributions in rods.

Physiological roles of PMP surface charge and negative disc membrane surface potential

Our results with acylated probes directly demonstrate that disc membranes in live cells bear a significant negative surface charge that impacts PMP dynamics under physiological conditions. This is consistent with previous in vitro results suggesting that the cytoplasmic surface charge of disc membranes, per rhodopsin, is between approximately −5 and −1.5, corresponding to a charge density of approximately (−)0.1 to (−)0.3 per square nanometer (Hubbell, 1990; Tsui et al., 1990; Hubbell et al., 2003). The potential physiological impact of the disc membrane surface charge on transducin disc association was addressed computationally by Kosloff et al. (2008), who showed that Tα has a significantly lower affinity to disc membranes than Tαβγ trimer owing to membrane repulsion of negative charges on Tα. Positive surface charge of Tβγ near the farnesyl site was proposed to result in substantially higher disc membrane affinity, enough so that Tαβγ trimer has a net disc membrane attraction (Kosloff et al., 2008). It is thought that Tα release from Tβγ may thus drive light-dependent Tα translocation to the IS (reviewed in Calvert et al., 2006) when the number of activated transducins rises above the level of GTPase activating complexes, RGS9-Gβ5-R9AP (Lobanova et al., 2007), possibly assisted by association with Unc119 (Zhang et al., 2011). Our results measuring membrane affinity of PMP probes in the OS support this idea. However, they also show that the acylated probe with the weakest membrane affinity (Myr-8) remains OS enriched and that Unc119 association with acylated Tαnt16-EGFP does not result in a distribution significantly different from Myr-8, suggesting additional unknown factors are involved in setting transducin distribution patterns in light- and dark-adapted rods.

The dependence of the affinity of charge-bearing PMPs on membrane surface potential leads to the possibility that binding strength changes depending on the light-adapted state of the photoreceptor. The membrane potential of dark-adapted rods, where a fraction of the OS cyclic nucleotide gated cation channels remain open, is depolarized to approximately −20 mV and the rod OS has a cytosolic Ca^{2+} concentration of 400–600 nM (McCarthy et al., 1994; Younger et al., 1996). In contrast, rods whose cyclic nucleotide gated channels are completely closed by strong light have a membrane potential of approximately −60 mV and cytosolic Ca^{2+} of a few nanomolar. Thus, PMPs may undergo a shift in membrane affinity due to changes in the concentrations of charge shielding cations, especially Ca^{2+}, or changes in the protein surface charge, e.g., by phosphorylation. Interestingly, GRK1 was reported to undergo light-dependent phosphorylation (Horner et al., 2005; Osawa et al., 2011), which would reduce its disc membrane affinity and thus reduce probability for activated rhodopsin encounter, possibly explaining the observed reduction in rhodopsin phosphorylation efficiency of phospho-GRK1 (Horner et al., 2005). Our ongoing work on imaging protein dynamics in dark- and light-adapted rods aims to explore these ideas.

Materials and methods

Generation of plasmid constructs and transgenic *X. laevis*

DNA constructs (Fig. S1) were generated using standard cloning and quickchange mutagenesis methods (Agilent). DNA sequences were placed downstream from the *X. laevis* opsin promoter to direct expression to rod photoreceptors (Mani et al., 2001). The coding region of each construct was sequenced (Genewiz) and the plasmid was linearized with XhoI endonuclease before restriction enzyme-mediated integration transgenics. Prior to oocyte injection, the plasmid was incubated with XhoI digested *X. laevis* sperm nuclei. Sperm nuclei were then treated with *X. laevis* egg extract, and oocytes were fertilized by injection with the sperm nuclei (Kroll and Amaya, 1996; Knox et al., 1998). Embryos were screened for epifluorescence in the eye, and transgenic animals were grown until eyes were large enough for retinal dissection (approximately stage 42 and older). All procedures and animal handling were performed per the Public Health Service Policy on Humane Care and Use of Laboratory Animals. Sex of animals used in experiments was not determined; thus, equal numbers of males and females were likely used.

Tissue preparation

X. laevis was dark-adapted for 2–12 h before imaging. Retina dissection was done with infrared illumination to minimize rhodopsin activation. Animals were bathed in 0.05% tricaine (ethyl 3-amino-benzoate methanesulfonate; Western Chemical) and decapitated. Eyes were removed and retinas dissected into frog Ringer's solution (120 mM NaCl, 2 mM KCl, 10 mM Hepes, 1.6 mM $MgCl_2$, 10 mM glucose, 0.03 mM EDTA, and 1.0 mM $CaCl_2$). Retinas were placed photoreceptor side up and sliced into strips (Najafi et al., 2012). Retinal "chips" were transferred to a custom-made imaging chamber as described previously (Peet et al., 2004; Calvert et al., 2010).

Confocal imaging

Quantitative imaging experiments were performed using a custom-built confocal/multiphoton microscope described previously (Peet et al., 2004; Calvert et al., 2007, 2010). Briefly, the microscope consists of an inverted stand (Nikon TE2000-U) into which collimated laser beams were introduced via an x-y galvanometer mirror system (Cambridge Technology). Focus was controlled by a piezo objective motor (Physik Instrumente). In confocal mode, E/PAGFP was excited by the 488-nm line of an argon-ion laser (Spectra-Physics 162-C). In two-photon mode, E/PAGFP was exited with a titanium:sapphire laser (Mai Tai HP; Spectra-Physics). The excitation *psf* was generated by overfilling the back aperture of a 60×/1.2 numerical aperture, water-immersion objective (Plan Apo VC; Nikon) with the expanded, collimated laser beans, which were thus focused to the diffraction limit within the specimen. Fluorescence emission was

detected using avalanche photodiodes (SPCM-AQR-14; PerkinElmer) in the descanned position. Laser intensities were modulated with neutral density wedges (Thorlabs) and/or a Pockels cell (302RM; Conoptics). Data acquisition and instrument control were achieved through a custom LabView system produced in collaboration with Michael Coleman of Coleman Technologies. All imaging was performed at room temperature (18–20°C).

Cells expressing EGFP probes were located via epifluorescence using a GFP cube (96343; Chroma Technology). Cells expressing PAGFP probes were detected via epifluorescence using a violet cube (11005v2; Chroma Technology). 3D confocal scans were performed with sampling frequencies of 0.05–0.26 µm in *xy* and a *z*-step of up to 0.2 µm. 3D confocal images of individual cells were obtained by image segmentation and fluorescence distributions were quantified using custom Matlab computer programs. No other image processing that would compromise fluorescence quantification, such as deconvolution, were performed on the image data. 3D volume renderings were generated using VolView (Kitware).

Determination of the *psf* intensity profile

Direct measurement of the *psf* profile in our confocal microscope was performed by scanning 0.1 µm diameter fluorescent microspheres (Peet et al., 2004; Calvert et al., 2007; Geneva et al., 2017). Fluorescence profiles of the microspheres were fitted with Gaussians, yielding standard deviations (σ) in *xy* and in *z* of σ_{xy} = 0.14 µm and σ_z = 0.56 µm. To estimate the EGFP or PAGFP photoconversion profile or the blurring by convolution, the *psf* intensity profile was approximated as a 3D Gaussian,

$$I_{psf}(x,y,z) = a \times exp\left(-\frac{(x^2+y^2)}{2\sigma_{x.y}^2}\right) \times \exp\left(-\frac{z^2}{2\sigma_z^2}\right), \quad (3)$$

where *a* is the intensity maximum at the 3D center of the profile. For this analysis we used a normalized *psf* profile where $\iiint_{xyz} I_{psf} = 1$.

Image and statistical analysis

Image segmentation was performed using custom Matlab programs to isolate individual rod photoreceptors from 3D images of retinal chips. A spline was drawn down the center of the rod photoreceptor, and fluorescence values were collected along this spline. To determine the approximate fluorescence in each compartment without the blurring on the edges of the cells and compartments due to the *psf*, the 90th to 100th percentile fluorescence intensity values for the synapse, myoid, and ellipsoid regions were averaged and normalized to the total fluorescence of the cell to get the relative concentration value. For cells expressing constructs with lipidation motifs, the nuclei were nearly empty, so the zero to 10th percentile fluorescence values were taken, again to avoid blurring from neighboring, brighter compartments. These values were then averaged. The OS is much larger than the other compartments of the rod, and thus not as susceptible to blurring, so the average of all OS fluorescence values along the spline was used. The value for each compartment in each cell was then corrected for sampling frequency and normalized to total cell fluorescence. Values were then plotted in a box plot in which the red line is the median, and the bottom and top of the box are the 25th and 75th percentiles, respectively. The whiskers extend to the most extreme data points that aren't considered outliers. Outliers are any values over the maximum whisker length, which is the length of the interquartile range. Outliers are indicated with a red +. The green asterisk indicates the average. Statistically significant differences and P values were determined with one-way ANOVA and the Tukey–Kramer multiple comparison procedure.

Fluorescence relaxation after photoactivation (FRAPa) and fluorescence relaxation after photobleaching (FRAPb) experiments

OS diffusion measurements were made by two different methods: FRAPa and FRAPb. In FRAPa experiments, probes encoding PAGFP were expressed in *X. laevis* rod photoreceptors. Cells expressing the probes were identified by epifluorescence. A rectangular strip in the OS was photoactivated with a Tai-sapphire laser tuned to 820 nm. Fluorescent relaxation throughout the OS was monitored over a time scale of tens of minutes. In FRAPb experiments, cells expressing the EGFP version of probes were bleached with a Tai-sapphire laser tuned to 920 nm, either in a rectangular strip in the OS or at the synapse. Fluorescence recovery was monitored over a time scale of tens of minutes.

Diffusion model fitting of OS FRAP experiments

To estimate axial diffusion coefficients of the probes in the ciliary OS, FRAP relaxation curves were fitted with the one-dimensional diffusion model (Theory Eq. A4; cf. Calvert et al. [2010]). FRAP results were normalized to the prebleach fluorescence level (FRAPb) or the peak of the photoactivated fluorescence (FRAPa). The model was then solved over a range of D_{OS} values and the results fitted to the data by root mean square error minimization (Calvert et al., 2007, 2010). Each cell was modeled individually to take into account variable OS length and variable bleaching or photoactivation patterns.

Immunoprecipitation and Western blotting

A GFP-trap kit (Chromotek) was used to immunoprecipitate EGFP probes and interacting proteins from transgenic *X. laevis* retinas. For farnesylated probes, Western blots were probed with PDE6D polyclonal antibody from Novus Biologicals (NBP1-32730) and Living Colors A.v. monoclonal antibody (JL-8; 632381) to recognize PrBPδ and EGFP, respectively. Several Unc119 antibodies were tested, including an Unc119 antibody that was made and generously provided by F. Haeseleer, University of Washington, Seattle, WA (Haeseleer, 2008), an Unc119 polyclonal antibody purchased from Novus Biologicals (NBP1-81708), and Unc119B polyclonal antibody purchased from Invitrogen (PA5-24504). None of these antibodies detected Unc119 in *X. laevis* retinas.

Mass spectrometry protein identification

To probe for potential LBC proteins, we performed mass spectrometry protein identification on GFP trap pulldowns.

Sample processing

Immunoprecipitated samples were digested using either the filter-aided sample preparation (FASP) (Wiśniewski et al., 2009) or the digestion in stage tip (iST) (Wei et al., 2014) procedure. For FASP, a mixture of Tris, pH 8.5, SDS, and DTT was added to the sample to a final concentration of 10 mM, 0.4% (wt/wt), and 10 mM. Disulfides were reduced by heating to 95°C for 5 min, and the samples were cooled to room temperature before being transferred to a 10-kD molecular weight cutoff ultrafiltration vessel (OD010C33; Pall). 200 µl of 8 M urea containing 100 mM Tris, pH 8.5, was added, and the filters were centrifuged to near dryness. Cysteine residues were alkylated with 50 mM iodoacetamide for 25 min in the dark, followed by centrifugation. The retained proteins were further washed with three aliquots of urea + Tris, followed by three washes of 50 mM ammonium bicarbonate. Trypsin was added at a ratio of 1:50 (enzyme: sample) in 40 µl of 50 mM ammonium bicarbonate, and digestion was allowed to proceed overnight at 37°C. The resulting peptides were collected in a clean tube, and the filter was washed using 50 µl of 0.5 M NaCl.

Peptides were desalted using mixed-mode cation exchange (MCX) stage tips (Rappsilber et al., 2003). 200-µl tips were packed with two cores of Empore MCX material (SDB-RPS, 3M, 2241) made using 14-gauge blunt needles. The sorbent was conditioned with acetonitrile (ACN), washed with solvent A (3% ACN in water with 0.2% trifluoroacetic acid [TFA]), up to 10 µg of sample loaded, washed twice with solvent A, washed once with solvent B (65% ACN in water with 0.1% TFA), and eluted using 65% ACN in water containing 5% (vol/vol) of ammonium hydroxide. The desalted peptides were dried in a SpeedVac vacuum concentrator.

When using the iST protocol, stage tips were made by heat sealing the bottom of 200-µl tips, and subsequently packing these with two cores of Empore MCX material. Up to 20 µg of protein was added to each tube, followed by addition of 10 M urea to a final concentration of 2 M. Tris(2-carboxyethyl)phosphine and chloroacetamide were added to a final concentration of 10 and 40 mM, and the reaction was allowed to proceed for 10 min. An equal volume of digestion buffer was added, containing 10% vol/vol ACN, 100 mM Tris, pH 8.5, and 200 ng of trypsin. The tops of the pipette tips were sealed with parafilm. The samples were digested at 37°C for 3 h in a warm air incubator.

Sample recovery and cleanup was performed by removing the parafilm, cutting off the heat-sealed bottoms, and placing the tips in clean 1.5-ml tubes whose lids had premade holes to accommodate the tips. The samples were acidified using 5% trifluoroacetic acid. After spinning through the sample, the MCX material was washed with 2× 50 µl of 0.2% TFA solution, and 60 µl of 65% ACN with 0.2% TFA. The tips were then placed in clean 1.5-ml tubes and the peptides eluted using 75 µl of 65% ACN with 5% ammonium hydroxide. The peptides were dried in a speed-vac.

Liquid Chromatography–Mass Spectrometry (LC-MS)

Samples were dissolved in water containing 2% ACN and 0.5% formic acid to ∼0.25 µg/µL. 2 µL (0.5 µg) was injected onto a pulled tip nano-LC column with 75-µm inner diameter packed to 10 cm with 5 µm C18 particles. The peptides were separated using a 60-min gradient from 3–28% ACN over 60 min, followed by a 7-min ramp to 85% ACN. The column was connected inline with the Orbitrap Lumos via a nanoelectrospray source operating at 2.2 kV. The mass spectrometer was operated in data-dependent top speed mode with a cycle time of 2.5 s. MS^1 scans were collected at 60,000 resolution with an automatic gain control (AGC) target of $6.0x10^5$ and maximum injection time of 50 ms. Higher-energy collisional dissociation fragmentation was used followed by MS^2 scans in the Orbitrap at 15,000 resolution with AGC target 1.0E4 and 100-ms maximum injection time.

Database search

The MS data were searched using SequestHT in Proteome Discoverer (version 2.2) against the *X. laevis* proteome from Uniprot, containing 42,878 sequences, concatenated with common laboratory contaminant proteins. Enzyme specificity for trypsin was set to semi-tryptic with up to two missed cleavages. Precursor and product ion mass tolerances were 10 ppm and 0.6 D, respectively. Cysteine carbamidomethylation was set as a fixed modification and methionine oxidation as a variable modification. The output was filtered using the Percolator algorithm with strict false discovery rate set to 0.01.

Online supplemental material

Videos 1 and 2 show 3D images of a rod expressing EGFP-Far+8, rotating in different directions. Images were acquired as described for Fig. 4. Voxel containing the 95th percentile (red) and 50th percentile (green) are shown. 3D rendering were performed in VolView. Video 3 shows a 3D image of another rod expressing EGFP-Far+8. Acquisition and processing were as described in Videos 1 and 2. Tables S1, S2, and S3 show mass spectrometry protein identification results from a gel band at the putative molecular weight of Unc119 and two GFP-trap pulldown experiments. Fig. S1 shows distributions of EGFP with neutral, nonlipidated linkers on the N and C termini of GFP. Fig. S2 shows scatter plots of probe distributions versus expression level.

Appendix

Theory

Here we describe a DBT model that was developed to evaluate the impact of diffusion, local active transport, and local binding on the transport kinetics and the steady-state distribution of molecules in rod photoreceptors. Below we address each process individually and then combine them into a single model.

Diffusion

The general diffusion equation is

$$\frac{\partial c}{\partial t} = D\nabla^2 c, \tag{A1}$$

where c is the concentration of diffusing substance, t is time, D is the diffusion coefficient, and ∇^2 is the Laplacian operator. The rod photoreceptor may be treated as a cylinder with variable area of cross section. In cylindrical coordinates, the general diffusion equation is

$$\frac{\partial c}{\partial t} = D_r\left(\frac{\partial^2 c}{\partial r^2} + \frac{1}{r}\frac{\partial c}{\partial r}\right) + D_\theta \frac{1}{r^2}\left(\frac{\partial^2 c}{\partial \theta^2}\right) + D_z\left(\frac{\partial^2 c}{\partial z^2}\right), \quad \text{(A2)}$$

where D_r, D_θ, and D_z are the diffusion coefficients in the indicated directions. We have previously shown that axial diffusion of E/PAGFP is significantly slower than radial and angular diffusion, $D_r \approx D_\theta >> D_z$. Thus, the derivatives in r and θ can be neglected, and diffusion and distribution of molecules in the rod may be approximated along one spatial dimension, z. Taking this into consideration, Eq. A2 reduces to

$$\frac{\partial c}{\partial t} = D_{ap}\frac{\partial^2 c}{\partial z^2}, \quad \text{(A3)}$$

where D_{ap} is the apparent axial diffusion coefficient within the cell. The area of cross-section of rods and the local diffusivity of molecules varies as a function of axial position. We previously derived the diffusion equation to account for these variations (Calvert et al., 2010),

$$\frac{\partial c(z,t)}{\partial t} = \frac{1}{A(z)}\frac{\partial\left[A(z)D(z)\frac{\partial c}{\partial z}\right]}{\partial z}. \quad \text{(A4)}$$

Local binding

In the case of diffusion with binding, we may write the modified diffusion equation (Eq. A3; cf. Eq. 14.2, Crank [1975]),

$$\frac{\partial c_f}{\partial t} = D_{ap}\frac{\partial^2 c}{\partial x^2} - \frac{\partial c_b}{\partial t}, \quad \text{(A5)}$$

where c_f is the concentration of free, diffusing molecules, and c_b is the concentration of bound, nondiffusing molecules.

Eq. A4 thus becomes

$$\frac{\partial c_f(z,t)}{\partial t} = \frac{1}{A(z)}\frac{\partial\left[A(z)D(z)\frac{\partial c_f}{\partial z}\right]}{\partial z} - \frac{\partial c_b}{\partial t}, \quad \text{(A6)}$$

or with rearrangement,

$$\frac{\partial c_f}{\partial t} + \frac{\partial c_b}{\partial t} = \frac{1}{A(z)}\frac{\partial}{\partial z}\left(A(z)D(z)\frac{\partial c_f}{\partial z}\right). \quad \text{(A7)}$$

Assuming that binding/unbinding is much faster than diffusion, the bound concentration may be treated as an algebraic function of the free concentration,

$$c_b = f(c_f).$$

Substituting Eq. A7 for c_b in Eq. A6,

$$\frac{\partial c_f}{\partial t} + \frac{\partial f(c_f)}{\partial t} = \frac{1}{A(z)}\frac{\partial}{\partial z}\left(A(z)D(z)\frac{\partial c_f}{\partial z}\right)$$

$$\frac{\partial c_f}{\partial t} + \frac{df(c_f)}{dc_f}\frac{\partial c_f}{\partial t} = \frac{1}{A(z)}\frac{\partial}{\partial z}\left(A(z)D(z)\frac{\partial c_f}{\partial z}\right)$$

$$\left[1 + \frac{df(c_f)}{dc_f}\right]\frac{\partial c_f}{\partial t} = \frac{1}{A(z)}\frac{\partial}{\partial z}\left(A(z)D(z)\frac{\partial c_f}{\partial z}\right)$$

$$\frac{\partial c_f}{\partial t} = \frac{1}{\left[1 + \frac{df(c_f)}{dc_f}\right]}\frac{1}{A(z)}\frac{\partial}{\partial z}\left(A(z)D(z)\frac{\partial c_f}{\partial z}\right). \quad \text{(A8)}$$

Eq. A8 represents a general result for a variable area of cross-section, variable diffusivity, diffusion, and binding system. Together, Eqs. A7 and A8 are a partial differential algebraic equation system.

Next consider binding described by a Langmuir isotherm,

$$f(c_f) = \frac{B \cdot c_f}{K_d + c_f}, \quad \text{(A9)}$$

where $K_d = k_{-1}/k_1$ and B is binding capacity. Then,

$$\frac{df(c_f)}{dc_f} = \frac{B \cdot K_d}{(K_d + c_f)^2} = R, \quad \text{(A10)}$$

where R represents the binding reaction. Substitution of Eq. A10 into Eq. A8 yields

$$\frac{\partial c_f}{\partial t} = \frac{1}{\left[1 + \frac{B(z)\cdot K_d(z)}{(K_d(z) + c_f)^2}\right]}\frac{1}{A(z)}\frac{\partial}{\partial z}\left(A(z)D(z)\frac{\partial c_f}{\partial z}\right)$$

$$= \frac{1}{[1 + R(z)]}\frac{1}{A(z)}\frac{\partial}{\partial z}\left(A(z)D(z)\frac{\partial c_f}{\partial z}\right). \quad \text{(A11)}$$

Note that in the case of invariant $D(z)$, Eq. A8 becomes

$$\frac{\partial c_f}{\partial t} = \frac{D}{[1 + R(z)]}\frac{1}{A(z)}\frac{\partial}{\partial z}\left(A(z)\frac{\partial c_f}{\partial z}\right). \quad \text{(A12)}$$

Eq. A12 states that the effective diffusion coefficient, $D_{ef} \equiv \frac{D}{(1+R)}$, is inversely proportional to the binding reaction, R. Thus, local binding to immobile sites leads to a reduction in mobility that can be quantified by measuring the impact of functional domains appended to E/PAGFP on estimates of D.

Active transport

Calvert et al. (2010) introduced a local active transport component to the one-dimensional diffusion model (Eq. A4). The approach was to introduce a component that moves molecules within a defined volume region in a defined direction and velocity. A variety of mechanisms could underlie such active transport, including advective fluid flow, motor protein-based transport, and other mechanisms resulting in anisotropic transport. The active transport component may be added to Eq. A11,

$$\frac{\partial c_f}{\partial t} = \frac{1}{\left[1 + \frac{B(z)K_d(z)}{(K_d(z) + c_f)^2}\right]}\frac{1}{A(z)}\frac{\partial}{\partial z}\left(A(z)D(z)\frac{\partial c_f}{\partial z}\right) - \frac{1}{A(z)}\frac{\partial(A(z)v(z)c_f)}{\partial z}, \quad \text{(A13)}$$

where $v(z)$ is the transport velocity of unbound molecules.

Boundary and initial conditions

Eq. A4, and the systems of Eqs. A7 and A11 or A7 and A13 were solved using the numerical method of lines (MOL; Schiesser, 1991; Schiesser and Griffiths, 2009) where the following boundary and initial conditions were applied:

$$\frac{\partial c_f(z=0,t)}{\partial z} = \frac{\partial c_f(z=L,t)}{\partial z} = 0, \tag{A14}$$

$$c_f(z,0) = c_0(z). \tag{A15}$$

Eq. A14 specifies no flux boundaries (homogeneous Neumann boundary conditions) at the presynapse ($z = 0$) and the ciliary OS tip ($z = L$). Eq. A15 specifies the initial distribution of molecules throughout the rod cell. The MOL is an established general algorithm for hyperbolic-parabolic (convection-diffusion, equations first order in t) partial differential equations (PDEs) in which the spatial (boundary value) independent variables are replaced with algebraic approximations. The resulting system of initial value ordinary differential equations (ODEs) is then solved numerically with a library ODE integrator. In the present case, the ODE integrator is ode15s from the Matlab library. Additional details about the MOL are available in Schiesser (2013). The Matlab routines are available from the corresponding author upon request.

Eqs. A13, A14, and A15 comprise the DBT model that allows evaluation of the impact of spatially variable diffusion, binding, and active transport on the dynamics and steady-state distributions of proteins along the length of the photoreceptor neuron.

Acknowledgments

We thank members of the Center for Vision Research for helpful discussions, Benjamin Wipper for work performed as a Summer Undergraduate Research Fellowship (SURF) student, Daisy Spoer for work performed as a Syracuse University Capstone student, Ebbing de Jong for mass spec analysis and Carla Dias for technical assistance. We thank the reviewers and editors for many helpful comments that have greatly improved the paper.

This work was supported by National Institutes of Health grants R01-EY018421 and R01-EY028303 (to P.D. Calvert), S10-OD023617 (to the State University of New York Upstate Medical University Proteomics Core) and an unrestricted grant to the State University of New York Upstate Medical University Department of Ophthalmology from Research to Prevent Blindness. We are grateful for support from the Lions Clubs of Central New York, District 20-Y1.

The authors declare no competing financial interests.

Author contributions: N.A. Maza: Data curation, Formal analysis, Investigation, Methodology, Validation, Visualization, Writing – original draft, Writing – review & editing. W.E. Schiesser: Formal analysis, Methodology, Validation, Writing – review & editing. P.D. Calvert: Conceptualization, Data curation, Formal analysis, Investigation, Methodology, Validation, Visualization, Funding acquisition, Project administration, Resources, Software, Supervision, Writing – original draft, Writing – review & editing.

Submitted: 4 June 2019
Revised: 1 August 2019
Accepted: 29 August 2019

References

Baehr, W. 2014. Membrane protein transport in photoreceptors: the function of PDEδ: the Proctor lecture. *Invest. Ophthalmol. Vis. Sci.* 55:8653–8666. https://doi.org/10.1167/iovs.14-16066

Baker, S.A., M. Haeri, P. Yoo, S.M. Gospe III, N.P. Skiba, B.E. Knox, and V.Y. Arshavsky. 2008. The outer segment serves as a default destination for the trafficking of membrane proteins in photoreceptors. *J. Cell Biol.* 183: 485–498. https://doi.org/10.1083/jcb.200806009

Bentley, M., and G. Banker. 2016. The cellular mechanisms that maintain neuronal polarity. *Nat. Rev. Neurosci.* 17:611–622. https://doi.org/10.1038/nrn.2016.100

Besharse, J.C., J.G. Hollyfield, and M.E. Rayborn. 1977. Turnover of rod photoreceptor outer segments. II. Membrane addition and loss in relationship to light. *J. Cell Biol.* 75:507–527. https://doi.org/10.1083/jcb.75.2.507

Breslow, D.K., E.F. Koslover, F. Seydel, A.J. Spakowitz, and M.V. Nachury. 2013. An in vitro assay for entry into cilia reveals unique properties of the soluble diffusion barrier. *J. Cell Biol.* 203:129–147. https://doi.org/10.1083/jcb.201212024

Calvert, P.D., K.J. Strissel, W.E. Schiesser, E.N. Pugh Jr., and V.Y. Arshavsky. 2006. Light-driven translocation of signaling proteins in vertebrate photoreceptors. *Trends Cell Biol.* 16:560–568. https://doi.org/10.1016/j.tcb.2006.09.001

Calvert, P.D., J.A. Peet, A. Bragin, W.E. Schiesser, and E.N. Pugh Jr. 2007. Fluorescence relaxation in 3D from diffraction-limited sources of PAGFP or sinks of EGFP created by multiphoton photoconversion. *J. Microsc.* 225:49–71. https://doi.org/10.1111/j.1365-2818.2007.01715.x

Calvert, P.D., W.E. Schiesser, and E.N. Pugh Jr. 2010. Diffusion of a soluble protein, photoactivatable GFP, through a sensory cilium. *J. Gen. Physiol.* 135:173–196. https://doi.org/10.1085/jgp.200910322

Crank, J. 1975. *The Mathematics of Diffusion.* Oxford University Press, Oxford.

Datta, P., C. Allamargot, J.S. Hudson, E.K. Andersen, S. Bhattarai, A.V. Drack, V.C. Sheffield, and S. Seo. 2015. Accumulation of non-outer segment proteins in the outer segment underlies photoreceptor degeneration in Bardet-Biedl syndrome. *Proc. Natl. Acad. Sci. USA.* 112:E4400–E4409. https://doi.org/10.1073/pnas.1510111112

Deretic, D., and J. Wang. 2012. Molecular assemblies that control rhodopsin transport to the cilia. *Vision Res.* 75:5–10. https://doi.org/10.1016/j.visres.2012.07.015

El-Husseini, A.E., S.E. Craven, D.M. Chetkovich, B.L. Firestein, E. Schnell, C. Aoki, and D.S. Bredt. 2000. Dual palmitoylation of PSD-95 mediates its vesiculotubular sorting, postsynaptic targeting, and ion channel clustering. *J. Cell Biol.* 148:159–172. https://doi.org/10.1083/jcb.148.1.159

Endicott, S.J., and M. Brueckner. 2018. NUP98 Sets the Size-Exclusion Diffusion Limit through the Ciliary Base. *Curr. Biol.* 28:1643–1650.e3.

Fukata, Y., and M. Fukata. 2010. Protein palmitoylation in neuronal development and synaptic plasticity. *Nat. Rev. Neurosci.* 11:161–175. https://doi.org/10.1038/nrn2788

Geneva, I.I., and P.D. Calvert. 2010. High-Resolution Frap of the Cilium-Localized Somatostatin Receptor 3 Reveals the Presence of a Lateral Diffusion Barrier at the Cilium Base. *Biophys. J.* 98:376a. https://doi.org/10.1016/j.bpj.2009.12.2029

Geneva, I.I., H.Y. Tan, and P.D. Calvert. 2017. Untangling ciliary access and enrichment of two rhodopsin-like receptors using quantitative fluorescence microscopy reveals cell-specific sorting pathways. *Mol. Biol. Cell.* 28:554–566. https://doi.org/10.1091/mbc.e16-07-0549

Grossman, G.H., R.F. Watson, G.J. Pauer, K. Bollinger, and S.A. Hagstrom. 2011. Immunocytochemical evidence of Tulp1-dependent outer segment protein transport pathways in photoreceptor cells. *Exp. Eye Res.* 93: 658–668. https://doi.org/10.1016/j.exer.2011.08.005

Haeseleer, F. 2008. Interaction and colocalization of CaBP4 and Unc119 (MRG4) in photoreceptors. *Invest. Ophthalmol. Vis. Sci.* 49:2366–2375. https://doi.org/10.1167/iovs.07-1166

Hagins, W.A., R.D. Penn, and S. Yoshikami. 1970. Dark current and photocurrent in retinal rods. *Biophys. J.* 10:380–412. https://doi.org/10.1016/S0006-3495(70)86308-1

Hancock, J.F., H. Paterson, and C.J. Marshall. 1990. A polybasic domain or palmitoylation is required in addition to the CAAX motif to localize

p21ras to the plasma membrane. *Cell.* 63:133–139. https://doi.org/10.1016/0092-8674(90)90294-O

Hanke-Gogokhia, C., Z. Wu, C.D. Gerstner, J.M. Frederick, H. Zhang, and W. Baehr. 2016. Arf-like protein 3 (ARL3) regulates protein trafficking and ciliogenesis in mouse photoreceptors. *J. Biol. Chem.* 291:7142–7155.

Hilgendorf, K.I., C.T. Johnson, and P.K. Jackson. 2016. The primary cilium as a cellular receiver: organizing ciliary GPCR signaling. *Curr. Opin. Cell Biol.* 39:84–92. https://doi.org/10.1016/j.ceb.2016.02.008

Hollyfield, J.G., J.C. Besharse, and M.E. Rayborn. 1977. Turnover of rod photoreceptor outer segments. I. Membrane addition and loss in relationship to temperature. *J. Cell Biol.* 75:490–506. https://doi.org/10.1083/jcb.75.2.490

Horner, T.J., S. Osawa, M.D. Schaller, and E.R. Weiss. 2005. Phosphorylation of GRK1 and GRK7 by cAMP-dependent protein kinase attenuates their enzymatic activities. *J. Biol. Chem.* 280:28241–28250. https://doi.org/10.1074/jbc.M505117200

Hu, Q., L. Milenkovic, H. Jin, M.P. Scott, M.V. Nachury, E.T. Spiliotis, and W.J. Nelson. 2010. A septin diffusion barrier at the base of the primary cilium maintains ciliary membrane protein distribution. *Science.* 329:436–439. https://doi.org/10.1126/science.1191054

Hubbell, W.L. 1990. Transbilayer coupling mechanism for the formation of lipid asymmetry in biological membranes. Application to the photoreceptor disc membrane. *Biophys. J.* 57:99–108. https://doi.org/10.1016/S0006-3495(90)82510-8

Hubbell, W.L., C. Altenbach, C.M. Hubbell, and H.G. Khorana. 2003. Rhodopsin structure, dynamics, and activation: A perspective from crystallography, site-directed spin labeling, sulfhydryl reactivity, and disulfide cross-linking. In *Advances in Protein Chemistry. Vol.* Vol. Vol. 63. Douglas C. Rees, editor. Academic Press, New York. 243–290.

Jensen, V.L., and M.R. Leroux. 2017. Gates for soluble and membrane proteins, and two trafficking systems (IFT and LIFT), establish a dynamic ciliary signaling compartment. *Curr. Opin. Cell Biol.* 47:83–91. https://doi.org/10.1016/j.ceb.2017.03.012

Johnson, R.S., H. Ohguro, K. Palczewski, J.B. Hurley, K.A. Walsh, and T.A. Neubert. 1994. Heterogeneous N-acylation is a tissue- and species-specific posttranslational modification. *J. Biol. Chem.* 269:21067–21071.

Jovanovic-Talisman, T., and A. Zilman. 2017. Protein Transport by the Nuclear Pore Complex: Simple Biophysics of a Complex Biomachine. *Biophys. J.* 113:6–14. https://doi.org/10.1016/j.bpj.2017.05.024

Kee, H.L., J.F. Dishinger, T.L. Blasius, C.J. Liu, B. Margolis, and K.J. Verhey. 2012. A size-exclusion permeability barrier and nucleoporins characterize a ciliary pore complex that regulates transport into cilia. *Nat. Cell Biol.* 14:431–437. https://doi.org/10.1038/ncb2450

Kerov, V., W.W. Rubin, M. Natochin, N.A. Melling, M.E. Burns, and N.O. Artemyev. 2007. N-terminal fatty acylation of transducin profoundly influences its localization and the kinetics of photoresponse in rods. *J. Neurosci.* 27:10270–10277. https://doi.org/10.1523/JNEUROSCI.2494-07.2007

Klenchin, V.A., P.D. Calvert, and M.D. Bownds. 1995. Inhibition of rhodopsin kinase by recoverin. Further evidence for a negative feedback system in phototransduction. *J. Biol. Chem.* 270:16147–16152. https://doi.org/10.1074/jbc.270.27.16147

Knox, B.E., C. Schlueter, B.M. Sanger, C.B. Green, and J.C. Besharse. 1998. Transgene expression in Xenopus rods. *FEBS Lett.* 423:117–121. https://doi.org/10.1016/S0014-5793(98)00018-0

Kokame, K., Y. Fukada, T. Yoshizawa, T. Takao, and Y. Shimonishi. 1992. Lipid modification at the N terminus of photoreceptor G-protein alpha-subunit. *Nature.* 359:749–752. https://doi.org/10.1038/359749a0

Kosloff, M., E. Alexov, V.Y. Arshavsky, and B. Honig. 2008. Electrostatic and lipid anchor contributions to the interaction of transducin with membranes: mechanistic implications for activation and translocation. *J. Biol. Chem.* 283:31197–31207. https://doi.org/10.1074/jbc.M803799200

Kroll, K.L., and E. Amaya. 1996. Transgenic Xenopus embryos from sperm nuclear transplantations reveal FGF signaling requirements during gastrulation. *Development.* 122:3173–3183.

Lobanova, E.S., S. Finkelstein, H. Song, S.H. Tsang, C.K. Chen, M. Sokolov, N.P. Skiba, and V.Y. Arshavsky. 2007. Transducin translocation in rods is triggered by saturation of the GTPase-activating complex. *J. Neurosci.* 27:1151–1160. https://doi.org/10.1523/JNEUROSCI.5010-06.2007

Lodowski, K.H., R. Lee, P. Ropelewski, I. Nemet, G. Tian, and Y. Imanishi. 2013. Signals governing the trafficking and mistrafficking of a ciliary GPCR, rhodopsin. *J. Neurosci.* 33:13621–13638. https://doi.org/10.1523/JNEUROSCI.1520-13.2013

Mani, S.S., S. Batni, L. Whitaker, S. Chen, G. Engbretson, and B.E. Knox. 2001. Xenopus rhodopsin promoter. Identification of immediate upstream sequences necessary for high level, rod-specific transcription. *J. Biol. Chem.* 276:36557–36565. https://doi.org/10.1074/jbc.M101685200

McCarthy, S.T., J.P. Younger, and W.G. Owen. 1994. Free calcium concentrations in bullfrog rods determined in the presence of multiple forms of Fura-2. *Biophys. J.* 67:2076–2089. https://doi.org/10.1016/S0006-3495(94)80691-5

Murray, D., N. Ben-Tal, B. Honig, and S. McLaughlin. 1997. Electrostatic interaction of myristoylated proteins with membranes: simple physics, complicated biology. *Structure.* 5:985–989. https://doi.org/10.1016/S0969-2126(97)00251-7

Najafi, M., N.A. Maza, and P.D. Calvert. 2012. Steric volume exclusion sets soluble protein concentrations in photoreceptor sensory cilia. *Proc. Natl. Acad. Sci. USA.* 109:203–208. https://doi.org/10.1073/pnas.1115109109

Neubert, T.A., and J.B. Hurley. 1998. Functional heterogeneity of transducin alpha subunits. *FEBS Lett.* 422:343–345. https://doi.org/10.1016/S0014-5793(98)00037-4

Neubert, T.A., R.S. Johnson, J.B. Hurley, and K.A. Walsh. 1992. The rod transducin alpha subunit amino terminus is heterogeneously fatty acylated. *J. Biol. Chem.* 267:18274–18277.

Norton, A.W., S. Hosier, J.M. Terew, N. Li, A. Dhingra, N. Vardi, W. Baehr, and R.H. Cote. 2005. Evaluation of the 17-kDa prenyl-binding protein as a regulatory protein for phototransduction in retinal photoreceptors. *J. Biol. Chem.* 280:1248–1256. https://doi.org/10.1074/jbc.M410475200

Osawa, S., R. Jo, Y. Xiong, B. Reidel, N. Tserentsoodol, V.Y. Arshavsky, P.M. Iuvone, and E.R. Weiss. 2011. Phosphorylation of G protein-coupled receptor kinase 1 (GRK1) is regulated by light but independent of phototransduction in rod photoreceptors. *J. Biol. Chem.* 286:20923–20929. https://doi.org/10.1074/jbc.M111.230904

Peet, J.A., A. Bragin, P.D. Calvert, S.S. Nikonov, S. Mani, X. Zhao, J.C. Besharse, E.A. Pierce, B.E. Knox, and E.N. Pugh Jr. 2004. Quantification of the cytoplasmic spaces of living cells with EGFP reveals arrestin-EGFP to be in disequilibrium in dark adapted rod photoreceptors. *J. Cell Sci.* 117:3049–3059. https://doi.org/10.1242/jcs.01167

Peitzsch, R.M., and S. McLaughlin. 1993. Binding of acylated peptides and fatty acids to phospholipid vesicles: pertinence to myristoylated proteins. *Biochemistry.* 32:10436–10443. https://doi.org/10.1021/bi00090a020

Peters, K.R., G.E. Palade, B.G. Schneider, and D.S. Papermaster. 1983. Fine structure of a periciliary ridge complex of frog retinal rod cells revealed by ultrahigh resolution scanning electron microscopy. *J. Cell Biol.* 96:265–276. https://doi.org/10.1083/jcb.96.1.265

Rainy, N., T. Etzion, S. Alon, A. Pomeranz, Y. Nisgav, T. Livnat, M. Bach, C.D. Gerstner, W. Baehr, Y. Gothilf, and H. Stiebel-Kalish. 2016. Knockdown of unc119c results in visual impairment and early-onset retinal dystrophy in zebrafish. *Biochem. Biophys. Res. Commun.* 473:1211–1217. https://doi.org/10.1016/j.bbrc.2016.04.041

Rappsilber, J., Y. Ishihama, and M. Mann. 2003. Stop and go extraction tips for matrix-assisted laser desorption/ionization, nanoelectrospray, and LC/MS sample pretreatment in proteomics. *Anal. Chem.* 75:663–670. https://doi.org/10.1021/ac026117i

Resh, M.D. 2016. Fatty acylation of proteins: The long and the short of it. *Prog. Lipid Res.* 63:120–131. https://doi.org/10.1016/j.plipres.2016.05.002

Schacher, S., E. Holtzman, and D.C. Hood. 1976. Synaptic activity of frog retinal photoreceptors. A peroxidase uptake study. *J. Cell Biol.* 70:178–192. https://doi.org/10.1083/jcb.70.1.178

Schiesser, W.E. 1991. *The numerical method of lines: Integration of partial differential equations.* Academic Press, San Diego, CA.

Schiesser, W.E. 2013. *Partial Differential Equation Analysis in Biomedical Engineering: Case Studies with Matlab.* Cambridge University Press, Cambridge, UK.

Schiesser, W.E., and G.W. Griffiths. 2009. *A compendium of partial differential equation models: method of lines analysis with MATLAB.* Cambridge University Press, New York. https://doi.org/10.1017/CBO9780511576270

Silvius, J.R., and F. l'Heureux. 1994. Fluorimetric evaluation of the affinities of isoprenylated peptides for lipid bilayers. *Biochemistry.* 33:3014–3022. https://doi.org/10.1021/bi00176a034

Sorokin, S. 1962. Centrioles and the formation of rudimentary cilia by fibroblasts and smooth muscle cells. *J. Cell Biol.* 15:363–377. https://doi.org/10.1083/jcb.15.2.363

Spencer, M., P.B. Detwiler, and A.H. Bunt-Milam. 1988. Distribution of membrane proteins in mechanically dissociated retinal rods. *Invest. Ophthalmol. Vis. Sci.* 29:1012–1020.

Thomas, S., K.J. Wright, S. Le Corre, A. Micalizzi, M. Romani, A. Abhyankar, J. Saada, I. Perrault, J. Amiel, J. Litzler, et al. 2014. A homozygous PDE6D mutation in Joubert syndrome impairs targeting of farnesylated INPP5E

protein to the primary cilium. *Hum. Mutat.* 35:137–146. https://doi.org/10.1002/humu.22470

Townes-Anderson, E., P.R. MacLeish, and E. Raviola. 1985. Rod cells dissociated from mature salamander retina: ultrastructure and uptake of horseradish peroxidase. *J. Cell Biol.* 100:175–188. https://doi.org/10.1083/jcb.100.1.175

Tsui, F.C., S.A. Sundberg, and W.L. Hubbell. 1990. Distribution of charge on photoreceptor disc membranes and implications for charged lipid asymmetry. *Biophys. J.* 57:85–97. https://doi.org/10.1016/S0006-3495(90)82509-1

Vieira, O.V., K. Gaus, P. Verkade, J. Fullekrug, W.L.C. Vaz, and K. Simons. 2006. FAPP2, cilium formation, and compartmentalization of the apical membrane in polarized Madin-Darby canine kidney (MDCK) cells. *Proc. Natl. Acad. Sci. USA.* 103:18556–18561. https://doi.org/10.1073/pnas.0608291103

Wang, J., and D. Deretic. 2014. Molecular complexes that direct rhodopsin transport to primary cilia. *Prog. Retin. Eye Res.* 38:1–19. https://doi.org/10.1016/j.preteyeres.2013.08.004

Wei, L., F. Hu, Y. Shen, Z. Chen, Y. Yu, C.-C. Lin, M.C. Wang, and W. Min. 2014. Live-cell imaging of alkyne-tagged small biomolecules by stimulated Raman scattering. *Nat. Methods.* 11:410–412. https://doi.org/10.1038/nmeth.2878

Wiśniewski, J.R., A. Zougman, N. Nagaraj, and M. Mann. 2009. Universal sample preparation method for proteome analysis. *Nat. Methods.* 6:359–362. https://doi.org/10.1038/nmeth.1322

Wright, Z.C., R.K. Singh, R. Alpino, A.F. Goldberg, M. Sokolov, and V. Ramamurthy. 2016. ARL3 regulates trafficking of prenylated phototransduction proteins to the rod outer segment. *Hum. Mol. Genet.* 25:2031–2044. https://doi.org/10.1093/hmg/ddw077

Ye, F., A.R. Nager, and M.V. Nachury. 2018. BBSome trains remove activated GPCRs from cilia by enabling passage through the transition zone. *J. Cell Biol.* 217:1847–1868. https://doi.org/10.1083/jcb.201709041

Younger, J.P., S.T. McCarthy, and W.G. Owen. 1996. Light-dependent control of calcium in intact rods of the bullfrog Rana catesbeiana. *J. Neurophysiol.* 75:354–366. https://doi.org/10.1152/jn.1996.75.1.354

Zhang, H., S. Li, T. Doan, F. Rieke, P.B. Detwiler, J.M. Frederick, and W. Baehr. 2007. Deletion of PrBP/delta impedes transport of GRK1 and PDE6 catalytic subunits to photoreceptor outer segments. *Proc. Natl. Acad. Sci. USA.* 104:8857–8862. https://doi.org/10.1073/pnas.0701681104

Zhang, H., R. Constantine, S. Vorobiev, Y. Chen, J. Seetharaman, Y.J. Huang, R. Xiao, G.T. Montelione, C.D. Gerstner, M.W. Davis, et al. 2011. UNC119 is required for G protein trafficking in sensory neurons. *Nat. Neurosci.* 14:874–880. https://doi.org/10.1038/nn.2835

Zhang, H., R. Constantine, J.M. Frederick, and W. Baehr. 2012. The prenyl-binding protein PrBP/δ: a chaperone participating in intracellular trafficking. *Vision Res.* 75:19–25. https://doi.org/10.1016/j.visres.2012.08.013

Zhao, X., J. Huang, S.C. Khani, and K. Palczewski. 1998. Molecular forms of human rhodopsin kinase (GRK1). *J. Biol. Chem.* 273:5124–5131. https://doi.org/10.1074/jbc.273.9.5124